

HI intensity mapping : a single dish approach

R.A. Battye¹, I.W.A. Browne¹, C. Dickinson¹, G. Heron¹, B. Maffei¹, A. Pourtsidou^{1,2}

¹*Jodrell Bank Centre for Astrophysics, School of Physics and Astronomy, University of Manchester, Oxford Road, Manchester M13 9PL, U.K.*

²*Dipartimento di Astronomia, Università di Bologna, via Ranzani 1, I-40127 Bologna, Italy*

4 September 2012

ABSTRACT

We discuss the detection of large scale HI intensity fluctuations using a single dish approach with the ultimate objective of measuring the Baryonic Acoustic Oscillations (BAO) and constraining the properties of dark energy. To characterise the signal we present 3D power spectra, 2D angular power spectra for individual redshift slices, and also individual line-of-sight spectra, computed using the S^3 simulated HI catalogue which is based on the Millennium Simulation. We consider optimal instrument design and survey strategies for a single dish observation at low and high redshift for a fixed sensitivity. For a survey corresponding to an instrument with $T_{\text{sys}} = 50$ K, 50 feed horns and 1 year of observations, we find that at low redshift ($z \approx 0.3$), a resolution of ~ 40 arcmin and a survey of $\sim 5000 \text{ deg}^2$ is close to optimal, whereas at higher redshift ($z \approx 0.9$) a resolution of ~ 10 arcmin and $\sim 500 \text{ deg}^2$ would be necessary - something which would be difficult to achieve cheaply using a single dish. Continuum foreground emission from the Galaxy and extragalactic radio sources are potentially a problem. In particular, we suggest that it could be that the dominant extragalactic foreground comes from the clustering of very weak sources. We assess its amplitude and discuss ways by which it might be mitigated. We then introduce our concept for a dedicated single dish telescope designed to detect BAO at low redshifts. It involves an under-illuminated static ~ 40 m dish and a ~ 60 element receiver array held ~ 90 m above the under-illuminated dish. Correlation receivers will be used with each main science beam referenced against an antenna pointing at one of the Celestial Poles for stability and control of systematics. We make sensitivity estimates for our proposed system and projections for the uncertainties on the power spectrum after 1 year of observations. We find that it is possible to measure the acoustic scale at $z \approx 0.3$ with an accuracy $\sim 2.4\%$ and that w can be measured to an accuracy of 16%.

Key words: cosmology:observations – cosmology:theory

1 INTRODUCTION

Precision cosmology is now a reality. Measurements of the Cosmic Microwave Background (CMB), Large-Scale Structure (LSS) and Type Ia supernovae have led the way in defining the standard cosmological model, one based on a flat Friedmann-Robertson-Walker Universe containing cold dark matter (CDM) and a cosmological constant, Λ , with densities relative to the present day critical density $\Omega_m \approx 0.27$ and $\Omega_\Lambda \approx 0.73$ (Riess et al. 1998; Perlmutter et al. 1999; Eisenstein et al. 2001; Percival et al. 2002; Komatsu et al. 2011). The standard model has just 6 parameters, but these can be expanded to constrain, rule out, or detect more exotic possibilities. One particular case is an expanded dark energy sector, often parameterised by the equation of state parameter $w = P/\rho$ for the dark energy (Copeland et al. 2006), or even the possibility of modifications to gravity (Clifton et al. 2011). Observations which can constrain the

dark sector are usually geometrical (standard rulers or candles), or based on constraining the evolution of structure (Weinberg et al. 2012).

The use of Baryonic Acoustic Oscillations (BAOs) to constrain w is now an established technique (Eisenstein et al. 1998; Eisenstein 2003). Originally applied to the Third Data Release (DR3) of the SDSS Luminous Red Galaxy (LRG) survey (Eisenstein et al. 2005), subsequent detections have been reported by a number of groups analysing data from 2dF (Cole et al. 2005), SDSS DR7 (Percival et al. 2010), WiggleZ (Blake et al. 2011), 6dF (Beutler et al. 2011) and BOSS (Anderson et al. 2012). All these have used redshift surveys performed in the optical waveband to select galaxies. The power spectrum of their three dimensional distribution is computed and, assuming that the power spectrum of the selected galaxies is only biased relative to the underlying dark matter distribution by some overall scale-independent constant, the acoustic scale can then be extracted. Present

sample sizes used for the detection of BAOs are typically $\sim 10^5$ galaxies, but there are a number of projects planned to increase this to $\sim 10^7$ – 10^8 using optical and near infrared (NIR) observations which would lead to increased levels of statistical precision (Abbott et al. 2005; Hawken et al. 2011; Laureijs et al. 2011; Schlegel et al. 2011).

It is possible to perform redshift surveys in the radio waveband, using 21cm radiation from neutral hydrogen (HI) to select galaxies which could provide improved confidence in the results from the optical/NIR. At present the largest surveys have only detected $\sim 10^4$ galaxies (Meyer et al. 2004), limited by the low luminosity of the 21cm line emission (Furlanetto et al. 2006), but there are a number of proposed instruments with large collecting area capable of increasing this substantially in the next decade (Abdalla & Rawlings 2005; Duffy et al. 2008; Abdalla et al. 2010). By the time the Square Kilometre Array (SKA)¹ is online redshift surveys of galaxies selected in the radio should have comparable statistical strength to those made in the optical/NIR. The advantage of doing both radio and optical surveys is that they will be subject to completely different systematics.

An intriguing possibility is the idea of using what has become known as 21cm intensity mapping. The fact that the 21cm line is so weak means that it requires $\sim 1 \text{ km}^2$ of collecting area to detect L_* galaxies at $z \sim 1$ in an acceptable period of time - this was the original rationale for the SKA (Wilkinson 1991). However, instruments with apertures of $\sim 100 \text{ m}$ size have sufficient surface brightness sensitivity to detect HI at higher redshift, but they will preferentially detect objects of angular size comparable to their resolution as pointed out in Battye et al. (2004). These objects will be clusters with masses 10^{14} – $10^{15} M_\odot$ and other large scale structure. Peterson et al. (2006) and Loeb & Wyithe (2008) suggested that the full intensity field $T(\theta, \phi, f)$ could be used to measure the power spectrum as a function of redshift directly (as is done for the CMB intensity fluctuations) if the smooth continuum emission, e.g. that from the Galaxy, can be accurately subtracted and any systematic instrumental artefacts, arising from the observational strategy, can be calibrated to sufficient accuracy. If these obvious difficulties can be mitigated, then this technique can be enormously powerful: the standard approach of detecting galaxies and then averaging them to probe large scale structure is inefficient in the sense that to detect the galaxies, at say 5σ , one throws away all but a fraction of the detected 21cm emission. Although this is not a problem in the optical, in the radio where the signal is much weaker one cannot afford to take this hit. In order to measure the power spectrum one is not trying to detect the actual galaxies, although this can lead to a plethora of other legacy science, and all the detected emission is related to the LSS structure. Chang et al. (2008) have shown that dark energy can be strongly constrained with a radio telescope significantly smaller, and cheaper, than the SKA.

Interferometric techniques naturally deal with some of the issues related to foregrounds and instrumental systematics. In particular, they can filter out more efficiently the relatively smooth and bright contaminating signals from the Galaxy and local signals such as the Sun, Moon and

ground. However, interferometers can be extremely expensive since they require electronics to perform the large number of correlations. In this paper we will present our ideas on the design of a single dish telescope and an analysis of its performance (BINGO; **B**AO from **I**ntegrated **N**eutral **G**as **O**bservations). Attempts have already been made to detect the signal using presently operational, single-dish radio telescopes, (Chang et al. 2010) and recent surveys of the local universe (Pen et al. 2008). It has been possible to make detections using cross correlation with already available optical redshift surveys, but not the detection of the crucial autocorrelation signal needed to probe cosmology using radio observations alone. The reasons for this are unclear, but they are likely to be due to a combination of the observations not been taken with this specific purpose in mind and the fact that the telescope and detector system are not sufficiently stable. Our philosophy in this paper will be to quantify the expected HI signal, quantify the contaminating foreground signals and then present our design for a system which will be sufficiently sensitive and stable for the BAO signal to be extracted.

2 CHARACTERISATION OF THE SIGNAL

In this section we will present some basic material on the 21cm line emission in order to characterize various aspects of the signal expected in a HI intensity mapping experiment.

2.1 Mean Temperature

One can compute the emitted brightness temperature of the 21cm line in a velocity width dv using

$$T_{\text{emit}} dv = \frac{\hbar c^3}{k} \frac{3A_{21}}{16f_{\text{emit}}^2} n_{\text{HI}} dl, \quad (1)$$

where k is Boltzmann's constant, T_{emit} is the HI brightness temperature, $f_{\text{emit}} \approx 1420.4 \text{ MHz}$ is the rest frame emission frequency for neutral hydrogen, n_{HI} is the number density of neutral hydrogen atoms, dl is the line of sight distance and A_{21} is the spontaneous emission coefficient of the 21cm transition. Equation (1) can be used to deduce the standard formula which relates the observed integrated flux from an object (typically a galaxy) with HI mass M_{HI} (Roberts 1974)

$$M_{\text{HI}} = \frac{2.35 \times 10^5 M_\odot}{1+z} \frac{S_{\text{obs}} dv}{\text{Jy km s}^{-1}} \left(\frac{d_L(z)}{\text{Mpc}} \right)^2, \quad (2)$$

where $d_L(z)$ is the luminosity distance.

This standard formula is for an isolated object. However, on the very largest scales relevant to us here it is more convenient to work with the brightness temperature. The mean observed brightness temperature due to the average HI density in the Universe is

$$\bar{T}_{\text{obs}}(z) = \frac{\bar{T}_{\text{emit}}(z)}{1+z} = \left(\frac{\hbar c^3}{k} \frac{3A_{21}}{16f_{\text{emit}}^2 M_{\text{H}}} \right) \left(\frac{\rho_{\text{HI}}(z)}{1+z} \right) \frac{dl}{dv}, \quad (3)$$

where M_{H} is the mass of the hydrogen atom and $\rho_{\text{HI}}(z)$ is the average density of HI at redshift z . The first term is just a combination of fundamental constants and measured experimental parameters, the second is a function of redshift and the final, relatively unfamiliar, term relates the line of

¹ www.skatelescope.org

sight distance to the recession velocity and is given by H_0^{-1} in the local Universe, where H_0 is the Hubble constant.

In order to compute the last term in Equation (3), let us consider the comoving volume element

$$\frac{dV}{dzd\Omega} = \frac{cr^2}{H(z)} = c \left(\frac{r}{1+z} \right)^2 \frac{(1+z)^2}{H(z)} = c [d_A(z)]^2 \frac{(1+z)^2}{H(z)}, \quad (4)$$

$$r(z) = c \int_0^z \frac{dz'}{H(z')}, \quad (5)$$

where $d_A(z) = r(z)/(1+z)$ is the angular diameter distance and . We can also write $dV = d_A^2 dl d\Omega$ and hence

$$\frac{dl}{dz} = \frac{c}{H(z)} (1+z)^2. \quad (6)$$

Therefore, using $dv/c = dz/(1+z)$, we find that

$$\frac{dl}{dv} = \frac{(1+z)^3}{H(z)}. \quad (7)$$

Hence, (3) becomes

$$\bar{T}_{\text{obs}}(z) = \left(\frac{3A_{21}\hbar c^3}{16f_{\text{emit}}^2 kM_H} \right) \frac{(1+z)^2 \rho_{\text{HI}}(z)}{H(z)}, \quad (8)$$

and substituting in values for the fundamental constants and re-writing $\rho_{\text{HI}}(z)$ in terms of the density relative to the present day critical density, $\Omega_{\text{HI}}(z) = 8\pi G\rho_{\text{HI}}(z)/(3H_0^2)$, gives

$$\bar{T}_{\text{obs}}(z) = 44\mu\text{K} \left(\frac{\Omega_{\text{HI}}(z)h}{2.45 \times 10^{-4}} \right) \frac{(1+z)^2}{E(z)}, \quad (9)$$

where $h = H_0/100 \text{ km sec}^{-1} \text{ Mpc}^{-1}$ and $E(z) = H(z)/H_0$.

Throughout we will assume that $\Omega_{\text{HI}}h = 2.45 \times 10^{-4}$ independent of redshift which is the value calculated from the local HI mass function measured by HIPASS (Zwaan et al. 2005). Both observational (Prochaska & Wolfe 2009) and theoretical arguments (Duffy et al. 2011) appear to suggest that there is no more than a factor of 2 change in density of neutral hydrogen over the range of redshifts relevant to intensity mapping. In the rest of the paper we will drop the ‘‘obs’’ subscript and use T to denote the observed brightness temperature.

2.2 3D power spectrum

The 3D HI power spectrum can be written as

$$[\Delta T_{\text{HI}}(k, z)]^2 = \bar{T}(z)^2 [b(k, z)]^2 \frac{k^3 P_{\text{cdm}}(k, z)}{2\pi^2}, \quad (10)$$

where $b(k, z)$ is the bias and P_{cdm} is the underlying dark matter power spectrum. We will assume, for the purposes of this discussion, that $b = 1$ independent of redshift, z , and scale k . Martin et al. (2012) find that this is a good assumption for scales $> 10h^{-1} \text{ Mpc}$ implying that, within the constraints of their survey, that HI galaxies trace the large-scale structure of the Universe. In Fig. 1 we plot the predicted 3D linear power spectrum of 21 cm fluctuations for $z = 0.28$ which corresponds to the case (A) discussed in section 3 - the spectrum at other values of z is virtually indistinguishable on this logarithmic scale except for the overall growth factor. At low k , large angular scales, the signal has a spectrum $T_{\text{HI}} \propto k^2$, which turns over around

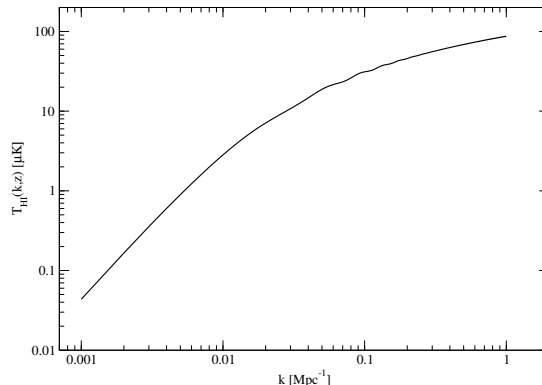


Figure 1. The 3D HI power spectrum at $z = 0.28$. BAOs are just about visible in the range $0.01 < k/\text{Mpc}^{-1} < 0.2$, but they are less than 10% of the total signal. For $k < 0.01 \text{ Mpc}^{-1}$ the temperature spectrum is $\propto k^2$ corresponding to $P(k) \propto k$, that is, scale invariant.

$k \sim 0.1 \text{ Mpc}^{-1}$. BAOs are less than 10% of the signal in the range $0.01 < k/\text{Mpc}^{-1} < 0.2$ and the power spectrum is significantly affected by the non-linear regime for $k > k_{\text{nl}}$ which is $\approx 0.2 \text{ Mpc}^{-1}$ at $z = 0$. The wavenumber k can be converted to angular multipole using $\ell \approx kr(z)$ where $r(z)$ is the coordinate distance and this can in turn be converted to an approximate angle scale using $\theta \approx 180 \text{ deg}/\ell$. The non-linear scale corresponds to $\ell_{\text{nl}} \approx 220$ and $\theta_{\text{nl}} \approx 0.8 \text{ deg}$ at low redshift ($z \approx 0.3$). Observations which probe significantly higher resolution than this will require the modelling of non-linear effects on the power spectrum. Note that this is somewhat different at higher redshifts.

2.3 2D Angular power spectrum

One can construct a 2D angular power spectrum for the HI intensity over some frequency range which can then be treated in using techniques designed to study the CMB anisotropies. We start from the 3D quantity $\delta\tilde{T}(r(z)\hat{\mathbf{n}}, z)$ which can be computed directly from (8) by replacing ρ_{HI} with $\delta\rho_{\text{HI}}$. This makes the assumption that dl/dv and $1+z$ take the values in an unperturbed universe, that is, we ignore the effects of peculiar velocities, which will lead to redshift space distortions that could be important on small scales, and the Sachs-Wolfe effects which could be important on large scales (Challinor & Lewis 2011; Bonvin & Durrer 2011). Its projection on the sky $\delta T(\hat{\mathbf{n}})$ is defined using a normalized projection kernel $W(z)$, that is

$$\begin{aligned} \delta T(\hat{\mathbf{n}}) &= \int dz W(z) \delta\tilde{T}(r(z)\hat{\mathbf{n}}, z) \\ &= \int dz W(z) \bar{T}(z) \delta_{\text{HI}}(r(z)\hat{\mathbf{n}}, z). \end{aligned} \quad (11)$$

We will use a top-hat projection kernel

$$W(z) = \begin{cases} \frac{1}{z_{\text{max}} - z_{\text{min}}} & \text{if } z_{\text{min}} \leq z \leq z_{\text{max}} \\ 0 & \text{otherwise,} \end{cases}$$

but the concept is more general and any weighting function could be used. The maximum and minimum redshifts of the bin are related to the minimum and maximum frequencies of the bin.

Fourier transforming and then expanding the Fourier modes in spherical harmonics, we have

$$\begin{aligned} \delta\tilde{T}(r(z)\hat{\mathbf{n}}, z) &= \bar{T}(z) \int \frac{d^3k}{(2\pi)^3} \hat{\delta}_{HI}(\mathbf{k}, z) e^{ir(z)\hat{\mathbf{n}}\mathbf{k}} \\ &= 4\pi\bar{T}(z) \sum_{l,m} i^\ell \int \frac{d^3k}{(2\pi)^3} \hat{\delta}_{HI}(\mathbf{k}, z) j_\ell(kr(z)) \\ &\quad \times Y_{\ell m}^*(\hat{\mathbf{k}}) Y_{\ell m}(\hat{\mathbf{n}}), \end{aligned} \quad (12)$$

where j_ℓ is the spherical Bessel function. We then have

$$\begin{aligned} \delta T(\hat{\mathbf{n}}) &= 4\pi \sum_{l,m} i^\ell \int dz W(z) \bar{T}(z) \\ &\quad \times \int \frac{d^3k}{(2\pi)^3} \hat{\delta}_{HI}(\mathbf{k}, z) j_\ell(kr(z)) Y_{\ell m}^*(\hat{\mathbf{k}}) Y_{\ell m}(\hat{\mathbf{n}}), \end{aligned} \quad (13)$$

which gives

$$a_{\ell m} = 4\pi i^\ell \int dz W(z) \bar{T}(z) \int \frac{d^3k}{(2\pi)^3} \hat{\delta}_{HI}(\mathbf{k}, z) j_\ell(kr(z)) Y_{\ell m}^*(\hat{\mathbf{k}}). \quad (14)$$

The angular power spectrum C_ℓ is found by taking the ensemble average

$$C_\ell \equiv \langle a_{\ell m} a_{\ell m}^* \rangle. \quad (15)$$

We need to use the orthonormality condition for the spherical harmonics, statistical isotropy and the definition of the power spectrum

$$\langle \hat{\delta}_{HI}(\mathbf{k}, z) \hat{\delta}_{HI}(\mathbf{k}', z') \rangle = (2\pi)^3 \delta(\mathbf{k} - \mathbf{k}') \delta^2 P_{\text{cdm}}(k) D(z) D(z'). \quad (16)$$

Here, $D(z)$ is the growth factor for dark matter perturbations defined such that $D(0) = 1$. Then we find that

$$\begin{aligned} C_\ell &= \frac{2b^2}{\pi} \int dz W(z) \bar{T}(z) D(z) \int dz' W(z') \bar{T}(z') D(z') \\ &\quad \times \int k^2 dk P_{\text{cdm}}(k) j_\ell(kr(z)) j_\ell(kr(z')). \end{aligned} \quad (17)$$

For large ℓ , we can use the Limber approximation (Limber 1953; Afshordi & Loverde 2008) to perform the k integral, that is,

$$\left(\frac{2}{\pi}\right) \int k^2 dk P_{\text{cdm}}(k) j_\ell(kr) j_\ell(kr') \quad (18)$$

$$= P_{\text{cdm}} \left(\frac{\ell + 1/2}{r} \right) \frac{\delta(r - r')}{r^2}. \quad (19)$$

Writing $cdz' = H_0 E(z') dr'$, we can use the δ -function to perform the dr' integral and we deduce

$$C_\ell = \frac{H_0 b^2}{c} \int dz E(z) \left[\frac{W(z) \bar{T}(z) D(z)}{r(z)} \right]^2 P_{\text{cdm}} \left(\frac{\ell + \frac{1}{2}}{r} \right). \quad (20)$$

We can proceed to calculate the 21cm angular power spectrum using (20). The matter power spectrum $P_{\text{cdm}}(k)$ today ($z = 0$) can be computed from

$$P_{\text{cdm}}(k) = A k^{n_S} T^2(k). \quad (21)$$

For the transfer function $T(k)$ we use the fitting formulae given by Eisenstein & Hu (1998), assuming $\Omega_m = 0.27$, $\Omega_\Lambda = 1 - \Omega_m$, $h = 0.71$ and baryon fraction $f_{\text{baryon}} = 0.17$. We take the primordial spectral index to be $n_S = 0.96$ and use the approximate formula by Bunn & White (1997) for

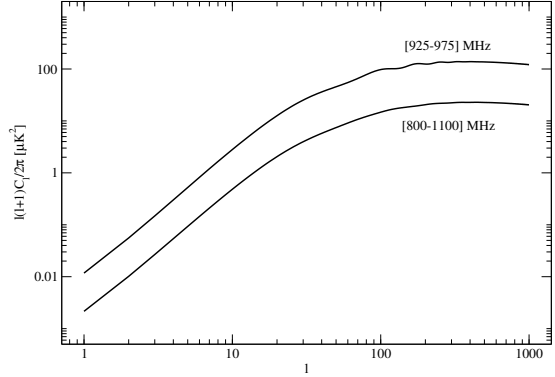


Figure 2. The HI angular power spectrum for the same central frequency, 950 MHz, but for two different ranges 925–975 MHz and 800–1100 MHz. The signal amplitude increases with decreasing the frequency range and the BAOs become more prominent. As the frequency range increases the size of the region probed becomes larger implying that the fluctuations will decrease.

the power spectrum amplitude. For this choice of parameters, the sound horizon $s \approx 152$ Mpc and the BAO scale $k_A = 2\pi/s \approx 0.041$ Mpc $^{-1}$. The growth function $D(z)$ is calculated using the fitting formula from Carroll, Press & Turner (1991).

In Fig. 2 we plot the HI angular power spectra for the same central frequency 950 MHz (corresponding to a central redshift $z_c \approx 0.5$) but for two different bin widths $\Delta f = 300$ MHz and $\Delta f = 50$ MHz. We see that as a result of decreasing the bin size, the signal amplitude increases and the BAO wiggles become more prominent. It is clear that there exists an optimum frequency bin size for which a detection will be possible: the signal-to-noise level would increase $\propto \sqrt{\Delta f}$ if the signal level was independent of frequency, but the level of fluctuations in the HI is reduced as the box enclosed by the angular beam-size and frequency range are increased. In Fig. 3 we plot the ratio $C_\ell/C_{\ell, \text{smooth}}$, where $C_{\ell, \text{smooth}}$ is the no-wiggles angular power spectrum (Eisenstein & Hu 1998) for the same central frequency 950 MHz but for the two frequency ranges used in Fig. 2. In addition we have plotted the ratio $P(k)/P_{\text{smooth}(k)}$, where $P(k) = P_{\text{cdm}}(k)$. Note that the ratio $C_\ell/C_{\ell, \text{smooth}}$ cannot be bigger than $P(k)/P_{\text{smooth}(k)}$. However, the two are in close agreement for the $\Delta f = 50$ MHz bin which indicates that this is the optimal frequency bin size for tracing the BAOs.

2.4 Estimated signal from S^3 simulations

Obreschkow et al. (2009a,b) present semi-analytic simulations of HI emission based on catalogues of galaxies whose properties are evolved from the Millennium or Milli-Millennium dark matter simulations (Springel et al. 2005) and we will use this to compute simulated spectra as would be observed by a single dish. We adopt the smaller of the two resultant mock sky fields (corresponding to the Milli-Millennium simulation, comoving diameter $s_{\text{box}} = 62.5 h^{-1}$ Mpc) for the characterisation of the expected HI signal which, as we will discuss later, restricts the highest redshift to which the spectrum will be complete. We extract galaxy properties from the simulated catalogue - position co-

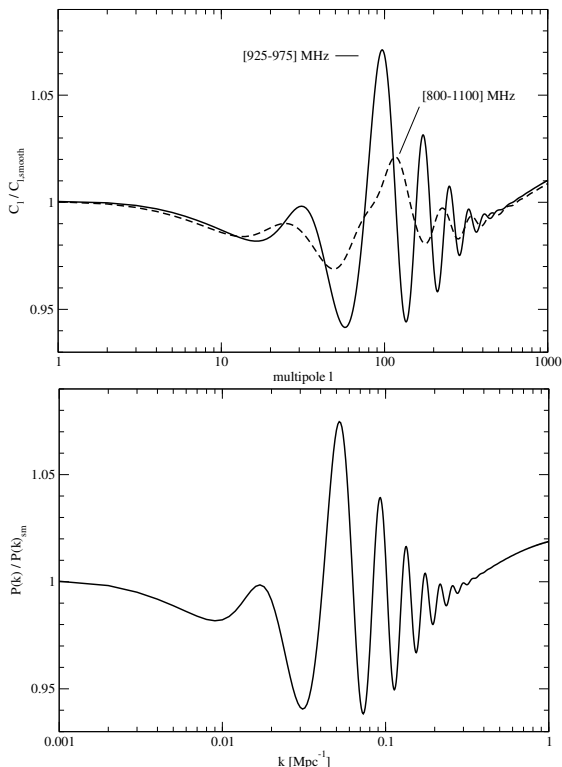
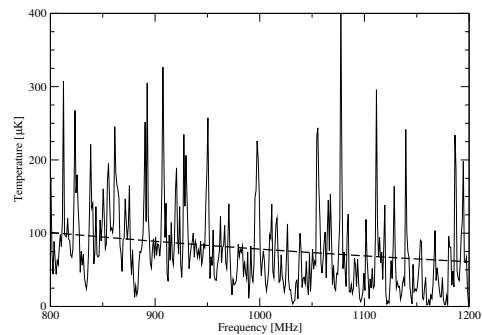


Figure 3. In the top plot we present the ratio $C_\ell/C_{\ell,\text{smooth}}$ for the same central frequency (950 MHz) but for different frequency ranges. In the bottom we present the ratio $P(k)/P(k)_{\text{smooth}}$. The 925 – 975 MHz curve in the upper plot is very similar to that in the lower one implying that a frequency range of 50 MHz will be optimal to detect the BAO signal at this redshift.

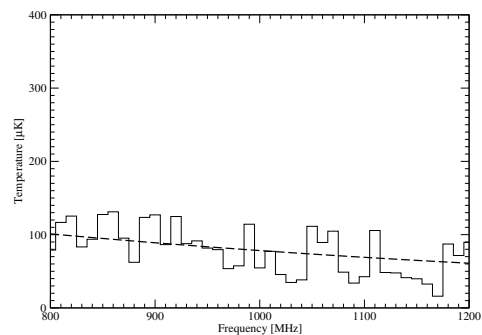
ordinates, redshift, HI mass, integrated HI flux and HI-line width - from which we calculate the HI brightness temperature contributed by galaxies in the frequency range Δf , as it would be observed by a telescope beam which is a top hat of diameter θ_{FWHM} independent of frequency. Using a diffraction limited beam for which $\theta_{\text{FWHM}} \propto 1 + z$ would result in a higher signal at lower frequencies.

In Fig. 4 we present the expected HI temperature fluctuations between frequencies of 800 and 1200 MHz, which is part of the frequency range we will be interested in, for a range of beam sizes, θ_{FWHM} and frequency bandwidths, Δf . These plots provide considerable insight into the nature of the signal that we will be trying to detect. It appears that the average signal from equation (9), represented by the dashed line, is compatible with the spectra from the Millennium Simulation. Larger values of θ_{FWHM} and Δf mean that the volume of the universe enclosed within a single cell is larger and hence the spectra have only very small deviations from the average, whereas for smaller values there are significant deviations as large as $400 \mu\text{K}$ illustrating that the signal on these scales can be much higher than the average.

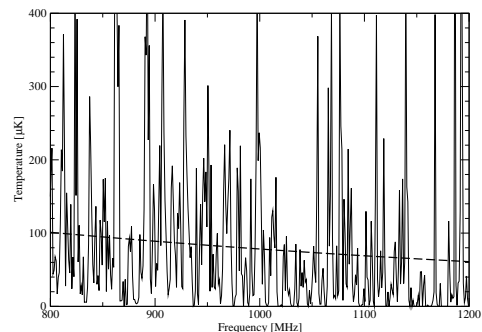
There are limitations to this approach: our spectra are not accurate out to arbitrarily high redshift where the cone diameter exceeds s_{box} and hence simulated catalogue is missing galaxies, that is, it is not complete. The maximum redshift for which the simulated catalogue is complete is determined by the beam size, with smaller beam sizes being



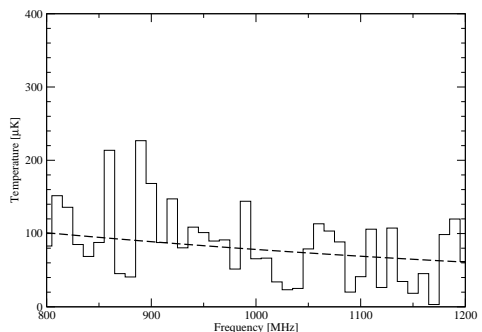
(a) $\Delta f = 1 \text{ MHz}, \theta_{\text{FWHM}} = 60 \text{ arcmin}$



(b) $\Delta f = 10 \text{ MHz}, \theta_{\text{FWHM}} = 60 \text{ arcmin}$



(c) $\Delta f = 1 \text{ MHz}, \theta_{\text{FWHM}} = 20 \text{ arcmin}$



(d) $\Delta f = 10 \text{ MHz}, \theta_{\text{FWHM}} = 20 \text{ arcmin}$

Figure 4. The simulated HI signal for different telescope beam resolution and frequency bin size combinations, θ_{FWHM} and Δf respectively. A smaller frequency bin or telescope beam size results in larger fluctuations, as expected, since going to smaller values of θ_{FWHM} and Δf means that one is probing a smaller volume of the Universe and fluctuations in the HI density are expected to be larger on smaller scales, as they are in the cold dark matter. In each case the dashed line is the average temperature computed using (9). The objective of 21cm intensity mapping experiments is to measure the difference between the signal and this average.

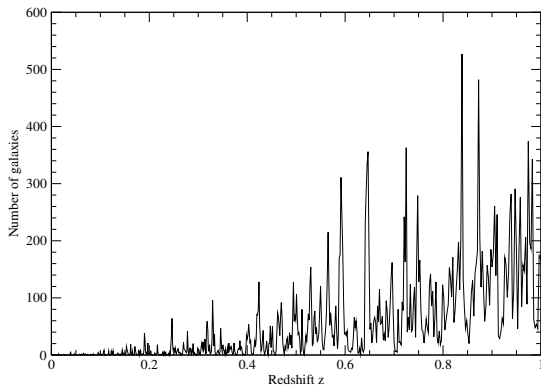


Figure 5. The number of galaxies contributing to the HI signal in each bin as a function of redshift. We have used $\theta_{\text{FWHM}} = 20$ arcmin and $\Delta f = 1$ MHz for this particular example. Note that the signal presented in Fig. 4 varies only very weakly with redshift yet the number of galaxies contributing to each bin increases dramatically. At low redshifts, we see that the signal is dominated by individual galaxies, at intermediate redshifts it is dominated by galaxy clusters and groups as suggested in Battye et al. (2004) and at high redshifts the signal comprises an unresolved background signal, that is, there are a very large number of galaxies contributing to each bin in redshift.

accurate to higher redshifts. For a beam size of 1° , the spectrum will be accurate up to around 600 MHz.

At the other end of the frequency range, which is not shown in Fig. 4, there are large fluctuations around the mean that can be attributed to the effects of shot noise. In Fig. 5, we plot the number of galaxies contributing to each bin of the spectrum defined by $\theta_{\text{FWHM}} = 20$ arcmin and $\Delta f = 1$ MHz, that is, Fig. 4(c), as a function of redshift. At low redshifts (high frequencies) the number of galaxies contributing to each bin is small, and the signal cannot be thought of as an unresolved background. If N is the number of contributing galaxies, the deviation due to shot noise is $\sigma^2 \propto 1/N$ and consequently, we see larger fluctuations. This is exactly the regime probed by surveys such as HIPASS and ALFALFA which detect individual galaxies for $z < 0.05$ with slightly better - but not substantially better - resolution than used in this plot. As one moves to higher redshifts a low resolution telescope will preferentially detect objects which have an angular size which is similar to that of the beam. At intermediate redshifts this will be the clusters discussed in Battye et al. (2004) and these can be clearly seen as the well-defined spikes in the spectrum around $z = 0.3 - 0.4$. At higher redshifts even clusters are beam-diluted; beyond $z = 0.5$ there are always a few galaxies contributing to each bin - essentially there is an unresolved background.

We can quantify the HI temperature fluctuations as a function of θ_{FWHM} and Δf by calculating their root mean squared (r.m.s.) deviation about the mean over the frequency range. As shown in Fig. 6, the r.m.s. decreases with increasing θ_{FWHM} and Δf . This is exactly what is expected since as θ_{FWHM} and Δf increase the region of the universe enclosed is larger and the observed temperature will become closer to the average. We note that typically the fluctuations are significantly bigger than one for a substantial part of the parameter space.

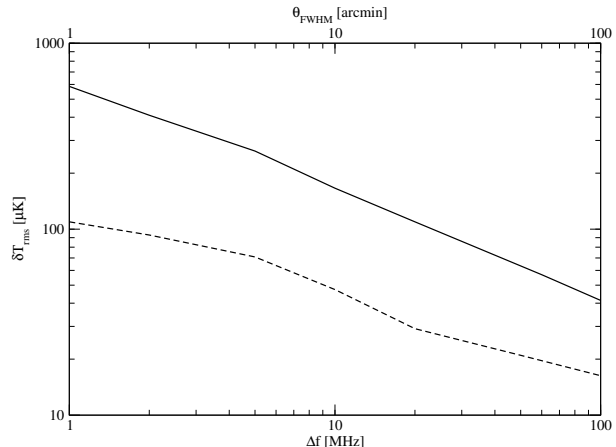


Figure 6. The r.m.s. temperature fluctuations in the HI signal as a function of θ_{FWHM} (solid line) and Δf (dashed line). When we vary θ_{FWHM} we fix $\Delta f = 1$ MHz and in the case where Δf is varied we fix $\theta_{\text{FWHM}} = 20$ arcmin.

3 OPTIMIZING THE PERFORMANCE AND SCIENCE POTENTIAL OF A SINGLE DISH EXPERIMENT

In this section we analyse the expected performance of a single dish telescope in two frequency ranges either side of the mobile phone band around 900–960 MHz: (A) $f = 960 - 1260$ MHz ($0.13 < z < 0.48$) and (B) $f = 600 - 900$ MHz ($0.58 < z < 1.37$). We will compute projected errorbars on the resulting power spectra based on the methods presented in Seo et al. (2010) using the 3D power spectrum (1). In each case, (A) and (B), we will optimize the area covered, Ω_{sur} , and the resolution of the telescope, $\theta_{\text{FWHM}} \propto 1/D$, where D is the illuminated area of the dish, in order to give the best possible measurement of the acoustic scale.

The standard expression for the projected error on a power spectrum measurement averaged over a radial bin in k -space of width Δk is (Feldman, Kaiser & Peacock 1994; Seo et al. 2010)

$$\frac{\sigma_P}{P} = \sqrt{2 \frac{(2\pi)^3}{V_{\text{sur}}} \frac{1}{4\pi k^2 \Delta k} \left(1 + \frac{\sigma_{\text{pix}}^2 V_{\text{pix}}}{[\bar{T}(z)]^2 W(k)^2 P} \right)}, \quad (22)$$

where we have neglected the contribution from shot noise. In order for the analysis to be simplified, it is necessary for us to make the errorbars on these so-called bandpower measurements uncorrelated. This requires that $\Delta k > \pi/(r(z)\theta_{\text{min}})$ where we assume that the observed sky area is a square patch with $\Omega_{\text{sur}} = \theta_{\text{min}} \times \theta_{\text{max}}$ and $\theta_{\text{max}} > \theta_{\text{min}}$. In order to be able to detect the acoustic scale we need Δk to be less than a few times k_A and this can impose important limitations on the design of drift scan surveys where typically $\theta_{\text{max}} \gg \theta_{\text{min}}$. V_{sur} is the survey volume given by

$$V_{\text{sur}} = \Omega_{\text{sur}} \int_{z_{\text{min}}}^{z_{\text{max}}} dz \frac{dV}{dz d\Omega}, \quad (23)$$

where

$$\frac{dV}{dz d\Omega} = \frac{cr(z)^2}{H_0 E(z)}. \quad (24)$$

The window function $W(k)$ models the instrument's angular and frequency response. Because our frequency resolution is relatively high, we can ignore the instrument response

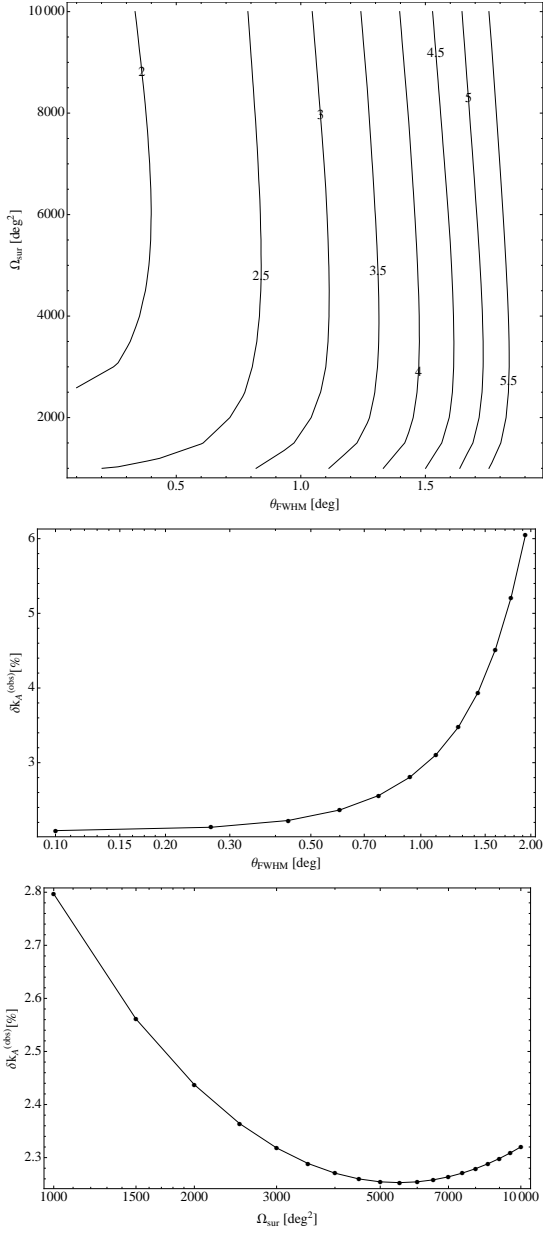


Figure 7. Optimization of the measurement of k_A for case (A) - observations over the frequency range 960 – 1260 MHz. We have computed the projected uncertainty on the measurement of k_A as a function of $\Delta\Omega_{\text{sur}}$ and the beam size θ_{FWHM} . In the top panel the contours are lines of constant δk_A with the numbers on the contours signifying the percentage fractional error: $100\delta_A/k_A$. In the middle panel we present a 1D slice as function of θ_{FWHM} with $\Delta\Omega_{\text{sur}} = 2000 \text{ deg}^2$ and in the bottom panel a 1D slice as a function of Ω_{sur} with $\theta_{\text{FWHM}} = 40 \text{ arcmin}$.

function in the radial direction. However, we have a finite angular resolution, which imposes a window function

$$W(k) = \exp\left[-\frac{1}{2}k^2 r(z)^2 \left(\frac{\theta_{\text{FWHM}}}{\sqrt{8\ln 2}}\right)^2\right]. \quad (25)$$

The beam area is given by $\Omega_{\text{pix}} \propto \theta_{\text{FWHM}}^2$ and the pixel volume is given by

$$V_{\text{pix}} = \Omega_{\text{pix}} \int_{z-\Delta z/2}^{z+\Delta z/2} dz \frac{dV}{dz d\Omega}, \quad (26)$$

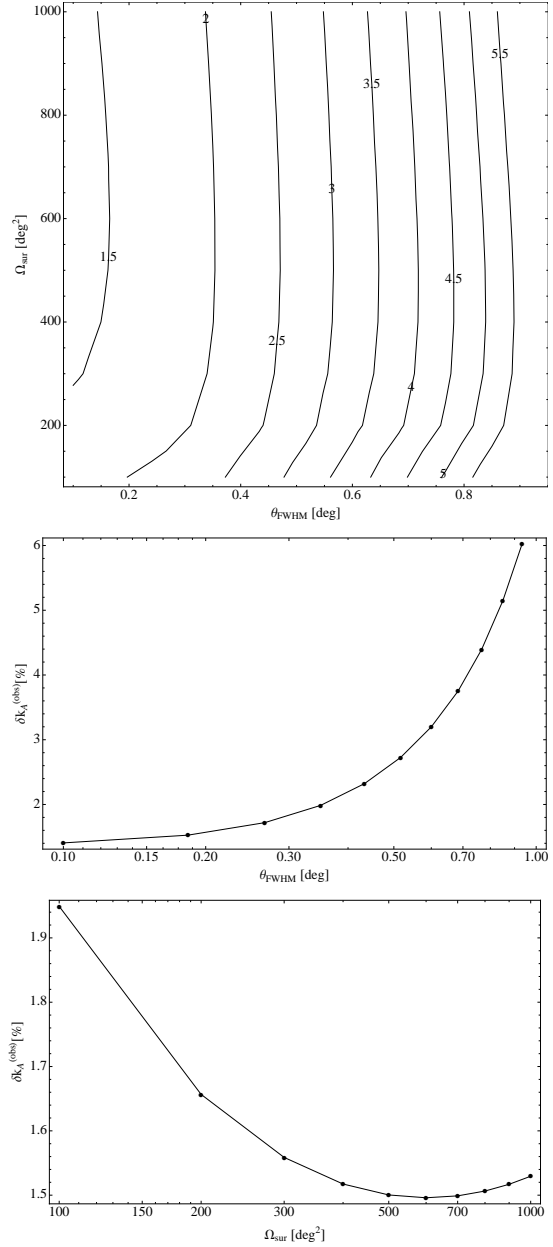


Figure 8. Optimization of the measurement of k_A for case (B) - observations over the frequency range 600 – 900 MHz. We have computed the projected error on the measurement of k_A as a function of $\Delta\Omega_{\text{sur}}$ and the beam size θ_{FWHM} . In the top panel the contours are lines of constant δk_A . The numbers on the contours are defined in the same way as in Fig. 7. In the middle panel we present a 1D slice as a function of θ_{FWHM} with $\Delta\Omega_{\text{sur}} = 500 \text{ deg}^2$ and in the bottom panel a 1D slice as a function of Ω_{sur} with $\theta_{\text{FWHM}} = 10 \text{ arcmin}$.

where Δz is the redshift range corresponding to Δf , the nominal frequency channel width, which we will take to be 1 MHz.

The pixel noise for a perfect, dual-polarisation, switch beam receiver measuring is given by

$$\sigma_{\text{pix}} = \frac{T_{\text{sys}}}{\sqrt{t_{\text{pix}} \Delta f}}, \quad (27)$$

where T_{sys} is the overall system temperature including con-

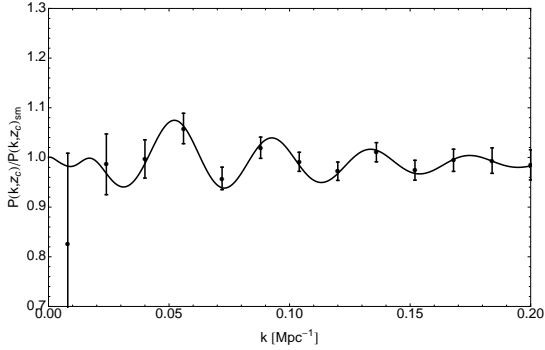


Figure 9. Projected errors on the power spectrum (divided by a smooth power spectrum) expected for the survey described by the parameters used in the text and Table 1 which is close the optimal value for Fig.7, that is, case (A) from Table 1. We have used $\Delta k = 0.016 \text{ Mpc}^{-1}$. The projected errors would lead to a measurement of the acoustic scale with a percentage fractional error of 2.4%. Note that the points do not lie on the line since they are band powers and hence are integrals over neighbouring values of k .

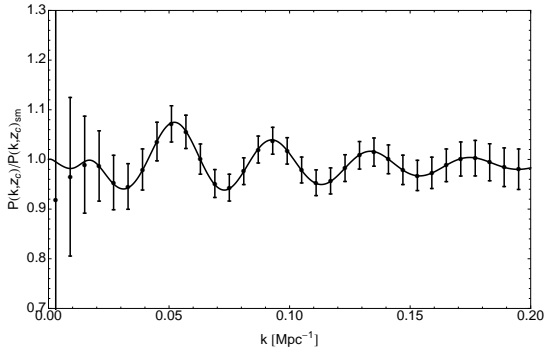


Figure 10. Projected errors on the power spectrum (divided by a smooth power spectrum) expected for the survey described by the parameters used in the text and table 1 which is close the optimal value for Fig.8, that is case (B) from table 1. We have used $\Delta k = 0.006 \text{ Mpc}^{-1}$. The projected errors would lead to a measurement of the acoustic scale with a percentage fractional error of 1.5%.

tributions from the sky, ground and receiver, which we will assume to be 50 K - a value that is conservative for a well designed system based on room temperature low noise amplifiers (LNAs) - and t_{pix} is the time spent observing one pixel. This is related to the total observing time, t_{obs} , by

$$t_{\text{obs}} = \frac{\Omega_{\text{sur}}}{n_{\text{F}} \Omega_{\text{pix}}} t_{\text{pix}}, \quad (28)$$

where n_{F} is the number of feedhorns at the focus of the telescope. In what follows we will keep t_{obs} and n_{F} fixed to be 1 year, that is a full year of on-source integration, something which may take around 2 years of elapse time to achieve, and 50, respectively. In order to estimate the error on the measurement of k_{A} we will follow Blake & Glazebrook (2003) and fit a decaying sinusoidal function to the projected data

$$\frac{P(k)}{P_{\text{ref}}} = 1 + Ak \exp \left[- \left(\frac{k}{0.1 h \text{ Mpc}^{-1}} \right)^{1.4} \right] \sin \left(\frac{2\pi k}{k_{\text{A}}} \right). \quad (29)$$

where the two parameters are the acoustic scale, k_{A} , and the overall amplitude, A , which we will ultimately marginalize over.

The parameter k_{A} is a function of the cosmological parameters and in particular the matter density measured relative to the critical density, Ω_{m} , and the equation of state parameter of the dark energy, $w = P_{\text{de}}/\rho_{\text{de}} = w_0 + w_1 z$. The angle-averaged power spectrum allows one to measure the isotropic BAO scale $k_{\text{A}} = (k_{\perp}^2 k_{\parallel})^{1/3}$ in terms of the wavenumbers parallel to, k_{\parallel} , and perpendicular to, k_{\perp} , the line-of-sight. An efficient and quick method to do this is to use the approximations (Seo & Eisenstein 2003; Glazebrook & Blake 2005)

$$k_{\parallel} = \frac{H(z)}{H^{\text{ref}}(z)} k_{\parallel}^{\text{ref}}, \quad k_{\perp} = \frac{d_{\text{A}}^{\text{ref}}(z)}{d_{\text{A}}(z)} k_{\perp}^{\text{ref}}, \quad (30)$$

in terms of reference values denoted by "ref" used for normalization purposes. Our reference cosmology is our input cosmology, with $w = -1 = \text{const}$, $\Omega_{\text{m}} = 0.27$ and $h = 0.71$. This allows us to define the angle-averaged distance to redshift z is given by (Beutler et al. 2011)

$$d_{\text{V}}(z) = \left(d_{\text{A}}(z)^2 \frac{cz(1+z)^2}{H(z)} \right)^{1/3}, \quad (31)$$

which takes into account the angular diameter distance, $d_{\text{A}}(z)$, and the radial distance $c/H_0 E(z)$.

In Figs. 7 and 8 we present projected percentage errors on the acoustic scale, $100\delta k_{\text{A}}/k_{\text{A}}$ as a function of the survey area, Ω_{sur} , and the beam size, θ_{FWHM} for the redshift ranges given by cases A and B. First it is clear that in each case there are a wide range of survey parameters for which accurate measurements of k_{A} can be made. It will always be the case that reducing θ_{FWHM} will lead to a better measurement of k_{A} . However, beyond some point one gets into a situation where there is a very significant extra cost for very little extra return.

In case A for $\Omega_{\text{sur}} > 2000 \text{ deg}^2$ the contours of constant $\delta k_{\text{A}}/k_{\text{A}}$ are almost vertical. This implies that for a fixed value of θ_{FWHM} , so long as one can achieve $\Omega_{\text{sur}} > 2000 \text{ deg}^2$, optimisation of the survey area can only yield minor improvements. This is illustrated in the bottom panel of Fig. 7, where we fixed θ_{FWHM} . The optimum Ω_{sur} is between 5000 and 6000 deg^2 where $\delta k_{\text{A}}/k_{\text{A}} \approx 0.0225$, but for example if $\Omega_{\text{sur}} = 2000 \text{ deg}^2$, as we will suggest for the BINGO instrument discussed in Section 5, $\delta k_{\text{A}}/k_{\text{A}} \approx 0.024$, a difference which is within the uncertainties of the present calculations. The exact position of the optimum is governed by a balance between cosmic variance and thermal noise terms in equation (22); typically, it is where the two are approximately equal. In the middle panel of Fig. 7 we fix $\Omega_{\text{sur}} = 2000 \text{ deg}^2$ and vary only θ_{FWHM} . There is a significant improvement in $\delta k_{\text{A}}/k_{\text{A}}$ as one goes from $\theta_{\text{FWHM}} = 2 \text{ deg}$ to around 40 arcmin but beyond that point there is little improvement. The reason for this is made apparent in Fig. 9 where we present the projected errors on $P(k)/P_{\text{smooth}}(k)$, where $P_{\text{smooth}}(k)$ is a smooth power spectrum chosen to highlight the BAOs. We see that as one goes to higher values of k , corresponding to higher angular resolution and lower values of θ_{FWHM} , the overall amplitude of the BAO signal decreases and therefore it is clear that the discriminatory power, in

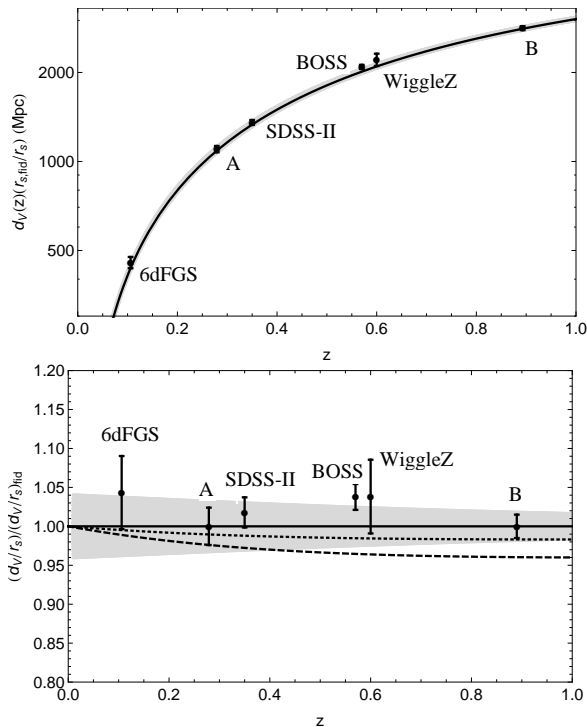


Figure 11. Projected constraints on the Hubble diagram for the volume averaged distance, $d_V(z)$, for cases A and B described by the parameters in table 1. Included also are the actual measurements made by 6dF, SDSS-II, BOSS and WiggleZ. The top panel is the absolute value and the bottom panel are the residuals from the fiducial model. On the bottom panel the shaded region indicates the range of d_V allowed by the 1σ constraint $\Omega_m h^2$ from WMAP7 (Komatsu et al. 2011). The dotted line is the prediction for $w_0 = -0.84$ (which could in principle be ruled out by case A) and the dashed line is $w_0 = -0.93$ (by case B).

terms of measuring BAOs² comes from the first three oscillations in the power spectrum. Although measuring beyond this point will improve the constraint, the improvement does not justify the substantial extra cost involved; going from $\theta_{\text{FWHM}} = 40$ arcmin to 20 arcmin would require the telescope diameter to increase by a factor of 2 and the cost by a factor of somewhere between 5 and 10. For the subsequent discussion of case A, we will concentrate on $\theta_{\text{FWHM}} = 40$ arcmin and $\Omega_{\text{sur}} = 2000 \text{ deg}^2$ and the relevant survey parameters are presented in Table 1. This is not exactly the optimum point in the $\theta_{\text{FWHM}} - \Omega_{\text{sur}}$ plane, but it is sufficiently close to the optimum. $\theta_{\text{FWHM}} = 40$ arcmin can be achieved with an illuminated diameter of around 25 m at the relevant frequencies and $\Omega_{\text{sur}} = 2000 \text{ deg}^2$ can be achieved with a drift scan strip of around 10 deg at moderate latitudes which is compatible with our choice of Δk . We note that the precise values of the optimum depend on the overall survey speed which is governed by $t_{\text{obs}} n_F / T_{\text{sys}}^2$. Typically an increase in the overall survey speed will move the optimum survey area to a larger value.

The situation for case (B) is qualitatively similar, but the exact values are somewhat different. Being centred at a

much higher redshift, $z \approx 0.9$, means that the angular size of the BAO scale is much smaller and hence higher resolution is necessary to resolve the BAO scale and a smaller area needs to be covered to achieve the same balance between thermal noise and cosmic variance. We find that something close to optimal can be achieved for $\theta_{\text{FWHM}} = 10$ arcmin and $\Omega_{\text{sur}} = 500 \text{ deg}^2$. The projected errors for such a configuration are displayed in Fig. 10 which would lead to $\delta k_A / k_A \approx 0.015$. In order to achieve this, one would need a single dish telescope with an illuminated diameter of ~ 100 m which would have to be steerable, at least in some way. It would be relatively expensive to build a dedicated facility to perform such a survey, although, of course, such facilities do already exist, albeit with very significant claims on their time from other science programs. Perhaps an interferometric solution could be used to achieve this optimum: we find that an array of ~ 250 antennas with a diameter of 4 m spread over a region of diameter ~ 100 m, having the same value T_{sys} , could achieve the same level of sensitivity. More generally an interferometer comprising n_d antennas of diameter D spread over a region of diameter d would be equivalent to a single dish of diameter d with a focal plane array with n_F feedhorns, if $n_d = d\sqrt{n_F}/D$ so long as $n_F < n_d$, that is the filling factor of the interferometer is < 1 .

In order to get an impression of the science reach of the proposed observations we have done two things. First, in Fig. 11 we have plotted our projected constraints on the angle-averaged distance on the BAO Hubble diagram - both absolute and residuals - along with the state-of-the-art measurements from 6dFGS, SDSS-II, BOSS and WiggleZ. It is clear that the measurements that would be possible from instruments capable of achieving the design parameters of cases A and B would be competitive with the present crop of observations and those likely to be done in the next few years. They would also be complementary in terms of redshift range and add to the possibility of measuring the cosmic distance scale solely from BAOs. We note that it should be possible, in fact, to make measurements of the acoustic scale over the full range of redshifts probed by the intensity mapping surveys and it would be possible to place a number of data points on the Hubble diagram, albeit with larger errorbars. In order to compare with the present surveys we decided to present a single data point.

In addition, we have made simple estimates of the projected errors of the dark energy parameters assuming that all the other cosmological parameters, including Ω_m are fixed. This will be a good approximation in the era of high precision CMB measurements made by, for example, the *Planck* Satellite³. For constant w , the measurement of $\delta k_A / k_A = 0.024$ possible in case A would lead to $\delta w / w = 0.16$, whereas for case B, where $\delta k_A / k_A = 0.015$ would lead to $\delta w / w = 0.07$. For models with non-constant w , we have performed a simple likelihood analysis for the two-dimensional parameter space $w_0 - w_1$ and the results are presented in Fig. 12 for cases A and B and a combination of the two. We see that since we have assumed a single redshift measurement of the acoustic scale, there is an exact

² We note that this might be different if we had chosen another science goal such as the measurement of neutrino masses.

³ We note that varying $\Omega_m h^2$ modifies $d_V(z)$ and the present limits on this parameter combination are included in Fig. 11. These will be substantially improved in the next couple of years.

Table 1. Table of the survey parameters used in Figs. 9 and 10. In both cases we have chosen the values of θ_{FWHM} and Ω_{sur} so as to be close the optimal values as described in the text. Included also are the projected measurements of the acoustic scale and estimates of the error w (assumed constant) when all other cosmological parameters are known.

Property	Low redshift (A)	High redshift (B)
z_{centre}	0.28	0.9
$r(z_{\text{centre}})$	1100 Mpc	3000 Mpc
Ω_{sur}	2000 deg ²	500 deg ²
V_{sur}	1.2 Gpc ³	3.1 Gpc ³
θ_{FWHM}	40 arcmin	10 arcmin
V_{pix}	810 Mpc ³	590 Mpc ³
r.m.s. noise level ($\Delta f = 1$ MHz)	85 μK	170 μK
$\delta k_{\Lambda}/k_{\Lambda}$	0.024	0.015
$\delta w/w$	0.16	0.07

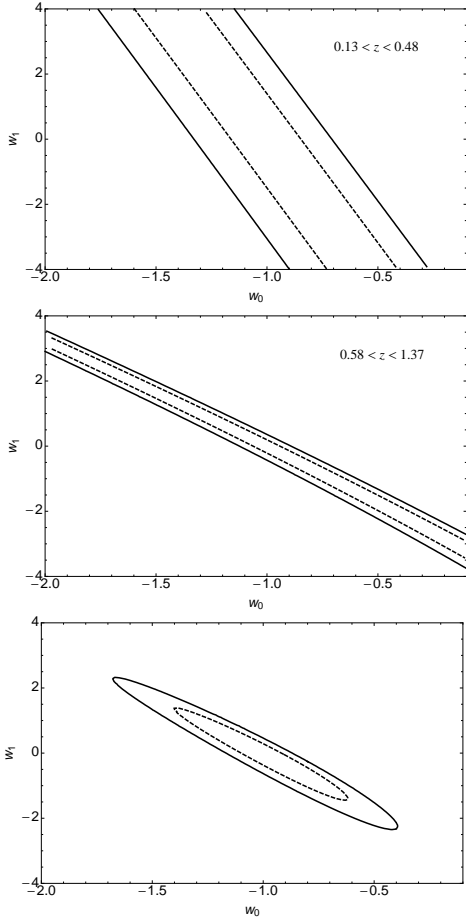


Figure 12. Projected uncertainties on the dark energy parameters w_0 and w_1 for case A with $\theta_{\text{FWHM}} = 2/3$ deg and $\Omega_{\text{sur}} = 2000$ deg² (top), case B with $\theta_{\text{FWHM}} = 10$ arcmin and $\Omega_{\text{sur}} = 500$ deg² (middle) and a combination of the two (bottom) for the case where all other cosmological parameters are known. We have assumed that cases A and B lead to a measurement of the acoustic scale at the central redshift of the survey which means that there is an absolute parameter degeneracy between the two parameters, but the degenerate line is different at the two redshifts. Combination of the two removes the degeneracy.

degeneracy between the two parameters, but the direction of the degeneracy is very different at the two different redshifts. When they are combined the degeneracy is broken and it is possible to estimate the two parameters separately.

4 FOREGROUND CONTAMINATION

4.1 Overview

To detect BAO in the faint HI signal, we will need to remove the contributions from much brighter foreground emission. The observed brightness temperature of the sky, $T_{\text{sky}}(f, \mathbf{x})$ at a frequency f and position \mathbf{x} , consists of several components

$$T_{\text{sky}}(f, \mathbf{x}) = T_{\text{CMB}}(f, \mathbf{x}) + T_{\text{gal}}(f, \mathbf{x}) + T_{\text{ps}}(f, \mathbf{x}) + T_{\text{HI}}(f, \mathbf{x}), \quad (32)$$

where T_{CMB} is the CMB temperature, T_{gal} is diffuse Galactic radiation, T_{ps} is emission from (mostly) unresolved extragalactic sources, and T_{HI} is the HI emission we are intending to detect. If the telescope and receiver are perfect, the total system temperature is given by $T_{\text{sys}} = T_{\text{sky}} + T_{\text{noise}}$ i.e. no other contributions (e.g. from ground-spillover) will add to T_{sys} .

The contribution from each foreground can be decomposed into a smooth component, $\bar{T}(f)$, and frequency and position varying fluctuations, $\delta T(f, \mathbf{x})$, about this smooth background

$$T(f, \mathbf{x}) = \bar{T}(f) + \delta T(f, \mathbf{x}). \quad (33)$$

The foregrounds will be much brighter than the HI signal, by several orders of magnitude. At $f = 1$ GHz, $\bar{T}_{\text{sky}} \sim 5$ K, while the HI brightness temperature is ~ 0.1 mK. However, our objective is to measure fluctuations of the sky brightness temperature as a function of both angular scale and redshift. Fluctuations of the HI signal are expected to be at the same level as the smooth component ($\delta T_{\text{HI}} \sim \bar{T}_{\text{HI}} \sim 0.1$ mK), while the fluctuations of the foregrounds will typically be much less ($\delta T \ll \bar{T}$). Furthermore, we can choose the coldest regions of sky to minimise the foreground signal. We will show that regions exist where the fluctuations in the foregrounds are in fact a little less than two orders of magnitude brighter than the HI signal. Given that the foregrounds will be smooth in frequency, this gives us confidence that foreground separation algorithms (e.g.

(Liu & Tegmark 2011)) can be employed that will allow a detection of BAO.

Estimates of the foreground brightness temperature fluctuations are presented in the next sections for each component and are summarised in Table 2.

4.2 Galactic synchrotron radiation

Synchrotron radiation is emitted by electrons spiralling in the Galactic magnetic field. The volume continuum emissivity is given by the integration of the power radiated by an electron $P(f; E)$ at a given energy E and frequency f , and the cosmic ray energy spectrum $N_e(E)$

$$\epsilon_f = \frac{1}{4\pi} \int_0^\infty P(f; E) N_e(E) dE. \quad (34)$$

The integration over a distribution of electrons, which itself is smooth, results in synchrotron spectra that are smooth, a property that we can exploit to separate synchrotron emission from hydrogen line emission.

At frequencies ~ 1 GHz observations indicate that synchrotron emission is well-approximated by a power-law with spectral indices in the range -2.3 to -3.0 (Reich & Reich 1988). The mean value $\beta \approx -2.7$ and mean dispersion $\sigma_\beta = 0.12$ are measured by Platania et al. (2003) in the range 0.4–2.3 GHz.

A number of large-area surveys are available at frequencies of ~ 1 GHz, most notably the all-sky 408 MHz map of (Haslam et al. 1982). We use the NCSA destriped and source-removed version of this map⁴ to estimate the contribution of synchrotron emission at 1 GHz. The 408 MHz map is extrapolated to 1 GHz using a spectral index of $\beta = -2.7$. The map is shown in RA-Declination coordinates in Fig. 13. The Galactic plane is evident as well as large-scale features that emit over large areas of the high latitude sky. The most prominent feature is the North Polar Spur which stretches over $\sim 100^\circ$ of the northern sky. The mean temperature at high Galactic latitudes ($|b| > 30^\circ$) is $T_{\text{sky}} \approx 2$ K with r.m.s. fluctuations in maps of 1° resolution of $\delta T_{\text{Gal}} \approx 530$ mK. The r.m.s. fluctuations are dominated by contributions from the large-scale features.

Fortunately, there exist large areas of low synchrotron temperature in the north. The declination strip at $\delta \sim +40^\circ$ is well known to be low in foregrounds (Davies et al. 1996) and is accessible by observing sites in the north. Furthermore, we are interested in the fluctuations at a given angular scale, or multipole value ℓ , rather than the r.m.s. value in the map at a given resolution. The r.m.s. estimate from the map will be considerably larger due to fluctuations on larger angular scales than the beam.

To estimate the foreground signal at a given ℓ -value we calculated the power spectrum of the $\delta = +45^\circ$ strip after masking out the Galactic plane ($|b| > 30^\circ$). This was achieved by using the POLSPICE⁵ software, which calculates the power spectrum from the 2-point pixel correlation function (Szapudi et al. 2001; Chon et al. 2004). We apodized the correlation function with a Gaussian of width $\sigma = 10^\circ$ to reduce ringing in the spectrum at the expense of smoothing

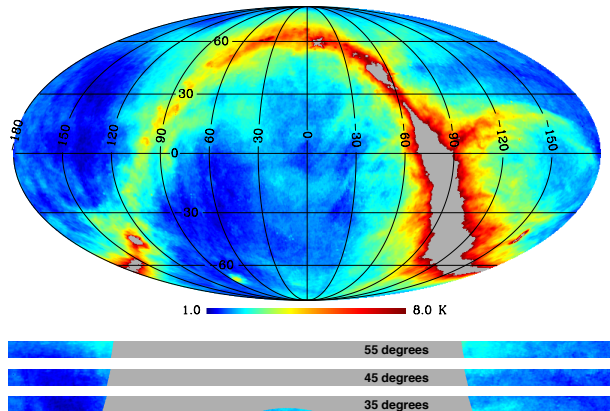


Figure 13. In the top plot, we present the entire synchrotron sky in celestial (RA/Dec) coordinates, with RA = 0° at the centre and increasing to the left. The map has been extrapolated from the all-sky 408 MHz map (Haslam et al. 1982) to 1 GHz using a spectral index $\beta = -2.7$ (Platania et al. 2003). The colour-scale is asinh from 1 K to 8 K. The saturated pixels ($T > 8$ K) are shown as grey. In the bottom plot, we present three drift scan strips, each 10° wide, located at declinations of 35° (bottom), 45° (middle) and 55° (top).

the spectrum. A power-law fit was then made to estimate the foreground signal at $\ell = 200$ ($\sim 1^\circ$). The result is given in Table 2.

For a 10° wide strip centred at $\delta = 45^\circ$ we find that the $\bar{T}_{\text{Gal}} = 1.7$ K with fluctuations of $\delta T_{\text{Gal}} = 67$ mK. Utilising these cool regions will be important for detecting the faint HI signal. The exact choice of strip will be a critical factor to be decided before construction of a fixed elevation telescope while the Galactic mask to be applied can be chosen during the data analysis step.

4.3 Free-free radiation

Free-free radiation (thermal bremsstrahlung) is emitted by electrons interacting with ions. At radio frequencies, this comes from warm ionized gas with typical temperatures of $T_e \sim 10^4$ K. Away from the Galactic plane, the radiation is optically thin and its brightness temperature is given by

$$T_{\text{ff}} \approx 90 \text{ mK} \left(\frac{T_e}{\text{K}} \right)^{-0.35} \left(\frac{f}{\text{GHz}} \right)^{-2.1} \left(\frac{\text{EM}}{\text{cm}^{-6} \text{ pc}} \right), \quad (35)$$

where EM is the emission measure representing the integral of the electron density squared along the line-of-sight ($\text{EM} = \int n_e^2 dl$). The free-free spectrum is therefore a well-defined power-law with a temperature spectral index $\beta = -2.1$ which acts to flatten the spectral index of the total continuum where it has a brightness temperature comparable to that of the synchrotron emission.

The EM can be estimated using $\text{H}\alpha$ measurements, which can then be converted to radio brightness temperature assuming T_e is known and the dust absorption is small (Dickinson et al. 2003). For $|b| > 30^\circ$, where $T_e \approx 8000$ K, $\text{EM} \sim 1.3 \text{ cm}^{-6} \text{ pc}$ at 1 GHz, this corresponds to $\bar{T}_{\text{ff}} \sim 5$ mK. For the 10° wide strip at $\delta = +45^\circ$ the free-free brightness temperature fluctuations are $\delta T_{\text{ff}} = 0.25$ mK at $\ell = 200$. The free-free component is therefore considerably weaker than the synchrotron component across most of the sky, but will act to (slightly) flatten the spectrum at higher frequencies.

⁴ <http://lambda.gsfc.nasa.gov/>

⁵ <http://www2.iap.fr/users/hivon/software/PolSpice/>.

Table 2. Summary of foregrounds for HI intensity mapping at 1 GHz for an angular scale of $\sim 1^\circ$ ($\ell \sim 200$). The estimates are for a 10° -wide strip at declination $\delta = +45^\circ$ and for Galactic latitudes $|b| > 30^\circ$.

Foreground	\bar{T} [mK]	δT [mK]	Notes
Synchrotron	1700	67	Power-law spectrum with $\beta \approx -2.7$.
Free-free	5.0	0.25	Power-law spectrum with $\beta \approx -2.1$.
Radio sources (Poisson)	–	5.5	Assuming removal of sources at $S > 10$ mJy.
Radio sources (clustered)	–	47.6	Assuming removal of sources at $S > 10$ mJy.
Extragalactic sources (total)	205	48	Combination of Poisson and clustered radio sources.
CMB	2726	0.07	Black-body spectrum, ($\beta = 0$).
Thermal dust	–	$\sim 2 \times 10^{-6}$	Model of Finkbeiner et al. (1999).
Spinning dust	–	$\sim 2 \times 10^{-3}$	Davies et al. (2006) and CNM model of Draine & Lazarian (1998).
RRL	0.05	3×10^{-3}	Hydrogen RRLs with $\Delta n = 1$.
Total foregrounds	~ 4600	~ 82	Total contribution assuming the components are uncorrelated.
HI	~ 0.1	~ 0.1	Cosmological HI signal we are intending to detect.

4.4 Extragalactic foregrounds

Extragalactic radio sources are an inhomogeneous mix of radio galaxies, quasars and other objects. These contribute an unresolved foreground⁶. The sources are often split into two populations based on their flux density spectral index, α ($S \propto \nu^\alpha$): steep spectrum sources with $\alpha < -0.5$ and flat spectrum sources with $\alpha > -0.5$. At low frequencies ($\lesssim 1$ GHz), steep spectrum sources with $\alpha \approx -0.75$ will dominate (Kellermann et al. 1968).

The contribution of point sources, T_{ps} , can be calculated from the differential source count, dN/dS , representing the number of sources per steradian, N , per unit flux, S . A number of compilations of source counts are available. We chose to use data collected from continuum surveys at 1.4 GHz data between 1985 and 2009, summarised in Table 3. Fig. 14 shows the Euclidean normalized differential source count for our compilation. We have fitted a 5th order polynomial to these data of the form

$$\log\left(\frac{S^{2.5}dN/dS}{N_0}\right) = \sum_{i=0}^5 a_i \left[\log\left(\frac{S}{S_0}\right)\right]^i, \quad (36)$$

where $N_0 = 1 \text{ Jy sr}^{-1}$ and $S_0 = 1 \text{ Jy}$ are normalizing constants. A least-squares fit gives the best-fitting coefficients: $a_0 = 2.593$, $a_1 = 0.093$, $a_2 = -0.0004$, $a_3 = 0.249$, $a_4 = 0.090$ and $a_5 = 0.009$. These values are compatible with those of Vernstrom et al. (2011).

Assuming we can subtract all sources with flux density $S > S_{\text{max}}$, we can calculate the mean temperature

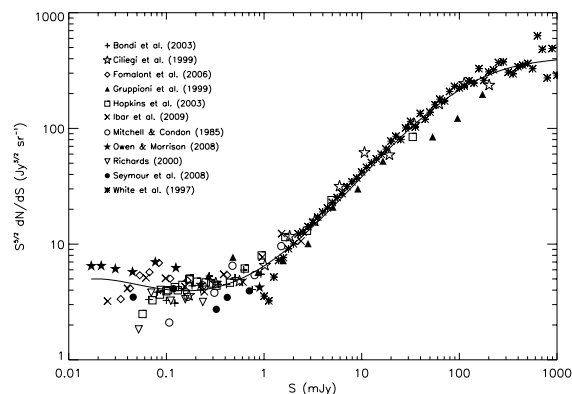
$$\bar{T}_{\text{ps}} = \left(\frac{dB}{dT}\right)^{-1} \int_0^{S_{\text{max}}} S \frac{dN}{dS} dS, \quad (37)$$

where $dB/dT = 2kf^2/c^2$, c is the speed of light and k is the Boltzmann constant. We find $\bar{T}_{\text{ps}} = 97 \text{ mK}$ at 1.4 GHz for $S_{\text{max}} = \infty$. We would expect to be able to subtract the brightest radio sources down to $S_{\text{max}} = 10 \text{ mJy}$ using the NRAO VLA Sky-Survey (NVSS) which is complete to 3.4 mJy (Condon et al. 1998) although there will be a residual contribution due to the variability of radio sources. Sub-

⁶ For convenience we refer to extragalactic sources as a foreground though both lower redshift (foreground) and higher redshift (background) sources will contaminate the HI signal.

Table 3. References used for source surveys at ~ 1.4 GHz used for compilation of source counts.

Reference
Bondi et al. (2003)
Ciliegli et al. (1999)
Fomalont et al. (2006)
Gruppioni et al. (1999)
Hopkins et al. (1999)
Ibar et al. (2009)
Mitchell & Condon (1985)
Owen & Morrison (2008)
Richards (2000)
Seymour et al. (2008)
White et al. (1997)

**Figure 14.** The compilation of differential radio sources counts at 1.4 GHz which we have used. The solid line is the best-fitting 5th order polynomial.

tracting sources stronger than 10 mJy reduces the mean temperature of $\bar{T}_{\text{ps}} = 83 \text{ mK}$ at 1.4 GHz. Although this is a useful thing to do, we clearly see that the bulk of the background temperature arising from extragalactic sources is contributed by the weakest ones and this is precisely the point where the uncertainty in the counts is greatest. Ex-

trapolating the course counts to 1 GHz with the mean temperature spectral index $\beta = -2.7$ gives $\bar{T}_{\text{ps}} = 205$ mK.

Before we continue, we note that there is evidence of an additional component to the sky brightness as measured by the ARCADE experiment at 3 GHz (Fixsen et al. 2011). They measured an excess component of radiation with a brightness temperature of ~ 1 K at 1 GHz and with a spectral index $\beta \approx -2.6$. Given the extreme difficulty in making absolute sky brightness measurements further observations, perhaps at lower frequency where the claimed excess is stronger, are required to firmly establish its reality. However, if it is real, this could require either a re-interpretation of Galactic radiation contributions or be evidence for a new population of extragalactic sources (Seiffert et al. 2011) - cf our point concerning the sensitivity of the computation of T_{ps} to the lower cut-off. For our initial analysis presented here, we do not consider this result further although we note that this could increase our foreground estimates significantly.

There are two contributions to δT_{ps} . The first is due to randomly (Poisson) distributed sources. However, if the sources have a non-trivial two-point correlation function, then there is a contribution due to clustering. We quantify the spatial fluctuations in δT_{ps} in terms of the angular power spectrum, $C_\ell = C_\ell^{\text{Poisson}} + C_\ell^{\text{clustering}}$, which is the Legendre transform of the two point correlation function $C(\theta)$.

Poisson distributed sources have a white power spectrum given by

$$C_\ell^{\text{Poisson}} = \left(\frac{dB}{dT} \right)^{-2} \int_0^{S_{\text{max}}} S^2 \frac{dN}{dS} dS. \quad (38)$$

In terms of multipoles, ℓ (where $\theta \sim 180^\circ/\ell$), the magnitude of the temperature fluctuations at any given angular scale is given by $\delta T = \sqrt{\ell(\ell+1)C_\ell/2\pi}$. Using our source count fit above to integrate up to $S_{\text{max}} = 10$ mJy and extrapolating to 1 GHz leads to fluctuations of $\delta T_{\text{ps}} = 5.5$ mK at $\ell = 200$ (1 deg)

The clustered component of radio sources acts to increase pixel-pixel correlations. The power spectrum due the clustered sources can be simply estimated as $C_\ell^{\text{cluster}} = w_\ell \bar{T}_{\text{ps}}^2$, where w_ℓ is the Legendre transform of the angular correlation function, $w(\theta)$ (Scott & White 1999). The clustering of radio sources at low flux densities (< 10 mJy) is not well-known. To make an estimate, we use $w(\theta)$ measured from NVSS, which can be approximated as $w(\theta) \approx (1.0 \pm 0.2) \times 10^{-3} \theta^{-0.8}$ (Overzier et al. 2003). Legendre transforming this gives $w_\ell \approx 4.8 \times 10^{-3} \ell^{-1.2}$. Although measured directly for sources at a higher flux density than those relevant here, the overall amplitude and power law are compatible with those expected if the galaxies follow clustering of cold dark matter.

The contribution to δT_{ps} at 1 GHz on angular scales $\sim 1^\circ$ from clustered sources, assuming a cut-off flux density of 10 mJy, is $\delta T_{\text{ps}} \approx 47.6$ mK. Plotting both the Poisson and clustering contributions to δT_{ps} , it can be seen in Fig. 15 that the contribution from the clustering component appears to be dominant over the Poisson fluctuations for multipoles $\ell < 500$ and is approximately an order of magnitude above the fluctuations in the HI signal.

The total contribution to δT_{ps} is then the quadrature sum of the Poisson and clustered components (they are uncorrelated), i.e. $C_\ell^{\text{ps}} = C_\ell^{\text{Poisson}} + C_\ell^{\text{clustering}}$ which leads

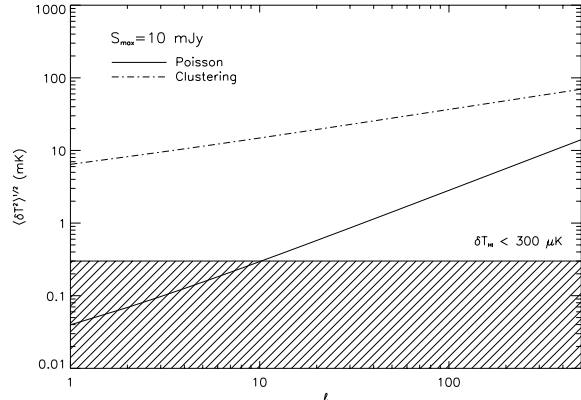


Figure 15. The Poisson and clustering contribution to the sky brightness temperature fluctuations for a flux cut-off value of $S_{\text{max}} = 10$ mJy. The brightness temperature fluctuations due to the 21 cm signal is expected to be $\lesssim 300 \mu\text{K}$ at redshifts $z \approx 0.5$ and is indicated by the hatched region.

to $\delta T_{\text{ps}} = \sqrt{\delta T_{\text{Poisson}}^2 + \delta T_{\text{cluster}}^2} \approx 48$ mK. We note that there is considerable uncertainty in this estimate, particularly with the clustered component. The extrapolation of our source count into the low flux density ($\ll 0.1$ mJy) regime may be unreliable (e.g. because the ARCADE results may imply an unexpectedly large population of very weak sources) and can only be firmly established by ultra-deep radio surveys with upcoming telescopes (e.g. Norris et al. (2011)).

4.5 Other foregrounds

A number of other foregrounds could also contribute to T_{sky} . Other diffuse continuum emission mechanisms include thermal dust and spinning dust emissions. Both of these are expected to be negligible at $\nu \sim 1$ GHz. For example, extrapolation of the thermal dust model of Finkbeiner et al. (1999), at 1° resolution predicts $\delta T \sim 2 \times 10^{-6}$ mK for $|b| > 30^\circ$. Similarly, extrapolating the anomalous microwave emission observed at 23 GHz by *WMAP* (Davies et al. 2006) and assuming it is all due to spinning dust emission from the cold neutral medium (CNM; Draine & Lazarian 1998), gives $\delta T \sim 2 \times 10^{-3}$ mK and can therefore be safely neglected.

There are a number of spectral lines which emit in the radio band. The most prevalent in the frequency range of interest are radio recombination lines (RRLs), primarily from hydrogen. The frequencies of these lines are given by the Rydberg equation, for example, H187 α is at a rest frequency of 997.63 MHz. The intensity of these lines can be estimated from the free-free continuum temperature, T_{ff} , using the following equation (Rohlfs & Wilson 2004)

$$\frac{\int T_L dV}{T_{\text{ff}} \Delta V} = 6.985 \times 10^3 \frac{1}{a(T_e)} \frac{1+n(\text{H})}{n(\text{He})} \left(\frac{T_e}{\text{K}} \right)^{-1.15} \left(\frac{\nu}{\text{GHz}} \right)^{1.1}, \quad (39)$$

where $a(T_e, \nu)$ is a correction factor, which at low frequencies is very close to 1 (Mezger & Henderson 1967). For a typical linewidth of 25 km s^{-1} , assuming $T_e = 8000$ K and a 8% helium to hydrogen ratio, the line temperature will be $\sim 1\%$ of the free-free continuum temperature at 1 GHz. Given the

estimates for Galactic foreground emission from Section 4.3, we expect $\bar{T}_L \sim 0.05$ mK and $\delta T_L \sim 2.5 \times 10^{-3}$ mK. Therefore, RRLs are not expected to be an important foreground either. Nevertheless, it would be wise to omit frequency channels that are known to contain the brightest ($\Delta n = 1$) hydrogen lines, which occur at intervals of approximately $\Delta f \approx 20$ MHz. We note, however, that these recombination lines contain much astrophysically interesting information about the Galaxy and therefore are likely to provide significant spin-off science from any radio BAO project.

5 THE BINGO CONCEPT

The discussion presented in Section 3 suggests that in order to get a good detection of BAO at low redshifts (case A from the optimisation study) a suitable single telescope should satisfy the following design constraints:

- an angular resolution defined by $\theta_{\text{FWHM}} \approx 40$ arcmin corresponding to an under-illuminated primary reflector with an edge taper < -20 dB;
- operate in the frequency range above 960 MHz with a bandwidth that is as wide as possible - exactly how wide and exactly where the band is positioned will ultimately be determined by those parts of the spectrum relatively free of radio frequency interference (RFI);
 - frequency resolution should be ~ 1 MHz or better;
 - frequency baseline should be as free as possible from instrumental ripples, particularly standing waves (Rohlfs & Wilson 2004);
- the receivers should be exceptionally stable in order to allow thermal-noise-limited integrations of a total duration long enough to reach a surface brightness limit $\sim 100 \mu\text{K}$ per pixel;
- the sky coverage as large as possible, but at the very least $> 2000 \text{ deg}^2$ with a minimum size in the smallest dimension of 10 deg;
 - the number of feeds should be $n_F > 50$ in order to achieve a sufficiently large signal-to-noise ratio;
 - sidelobe levels as low as possible so as to minimize the pickup of RFI and emission from strong sources;
 - beam ellipticity < 0.1 in order to allow map-making and power spectrum analysis routines to work efficiently;

For reasons of stability, simplicity, and cost, a telescope with no moving parts would be very desirable. We suggest that the following conceptual design could deliver what is required. We first concentrate on the telescope and then on the receiver design. We have named the overall project BINGO which stands for **BAO** from **I**ntegrated **N**eutral **G**as **O**bservations.

5.1 The telescope and focal plane

Operation at frequencies between 960 MHz and 1260 MHz is a practical possibility because it avoids strong RFI from mobile phone down-links which occupy the band up to 960 MHz. In order to achieve the desired resolution (better than 40 arcmin at 1 GHz), an under-illuminated primary reflector

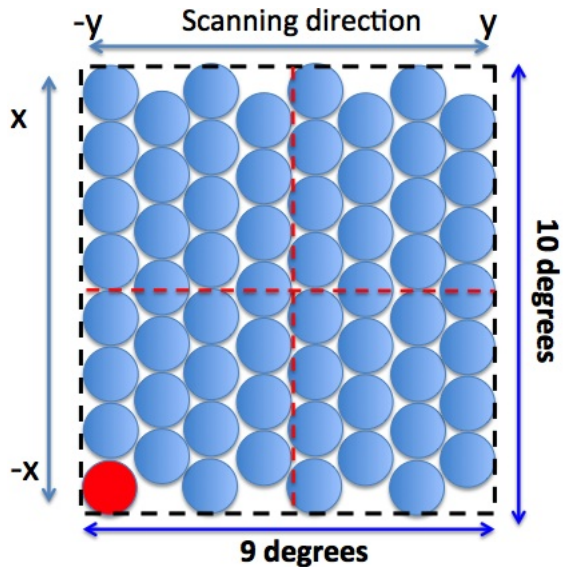


Figure 16. Focal plane of staggered feeds. A total of 60 pixels laid out in a rectangle (dashed black line) of $16 \text{ m} \times 15 \text{ m}$. This will allow for a FOV of about $10 \times 9 \text{ deg}^2$. Axes x and y are shown as a reference to the positions mentioned in Table 4. The pixel shown in red is the off-axis pixel corresponding to the beam profiles in Fig. 17.

of about 40 m projected aperture diameter, D , is required⁷. If the telescope is to have no moving parts, i.e. fixed pointing relative to the ground, then a wide instantaneous field-of-view (FOV) with multiple feeds is essential so that as the Earth rotates a broad strip of sky can be mapped during the course of a day. To reach the target sensitivity, a minimum number of 50 pixels is required in the focal plane, each of them reaching the following performance:

- Forward gain loss in comparison to central pixel < 1 dB;
- Cross-polarisation better than -30 dB;
- Beam ellipticity lower than about 0.1.

We propose to adopt an offset parabolic design in order to avoid blockage, minimise diffraction and scattering from the struts, and also to avoid standing waves that might be created between the dish and the feeds. A wide FOV with the required optical performance mentioned above can only be achieved with a long focal length. We found that a focal length $F = 90$ m, giving a focal ratio $F/D = 2.3$, much larger than more conventional radio telescopes (having typically a F/D ratio of about 0.4), is suitable for our purpose. This has the drawback of requiring the use of feeds with a small full-width-half-maximum, therefore with a large aperture diameter. For our telescope design, this means feeds with an aperture diameter of at least 2 m producing an edge taper telescope illumination of -20 dB in order to reduce the spillover. We are targeting a spillover of less than 2% in total power as the fraction of the horn beam not intercepting the telescope will see radiation from the ground therefore increasing the system temperature T_{sys} .

The design adopted for the focal plane is given in Fig. 16. A line of eight feeds allows for coverage of a 10 deg

⁷ The equivalent fully illuminated aperture would be $D \approx 25$ m

Table 4. Optical performance calculated using GRASP assuming ideal telescope and Gaussian feeds with -20 dB edge taper. Results are given for a pixel that would be located at the centre of the focal plane and for the corner edge pixel (red in Fig. 16 at $x = -8\text{ m}; y = -7.5\text{ m}$). Peak cross-polarisation is given respectively to the co-polarisation forward gain.

Pixel Position	Forward Gain	Ellipticity	Peak X-Pol	FWHM
	dB		dB	arcmin
Centre	49.8	10^{-3}	-40	38
Edge	49.6	0.07	-35	39

Table 5. Summary of proposed BINGO telescope parameters.

Reflector diameter	40 m
Resolution (at $\lambda = 30\text{ cm}$)	40 arcmin
Number of feeds	60
Instantaneous field of view	10 deg \times 9 deg
Frequency range	960 MHz to 1260 MHz
Number of frequency channels	≥ 300

strip. Along the scanning direction produced by the Earth’s rotation, other lines of feeds are staggered to allow for a proper sampling on the sky. With this configuration, 60 pixels, 10 more than the requirement, will produce a $10 \times 9\text{ deg}^2$ FOV. Assuming a feed aperture diameter of about 2 m, the resulting focal plane will be comprised within a rectangle of $16\text{ m} \times 15\text{ m}$.

Optical simulations of such a concept have been performed using Physical Optics (GRASP from TICRA) in order to take into account the diffraction effects. Results from this model, assuming ideal components (perfect telescope and Gaussian feedhorns) and a perfect alignment, are given in Table 4. The performance is well within the requirements even for the most off-axis pixel (represented in red in Fig. 16). Fig. 17 represents the modelled contour plot of the beams (co- and cross-polarisation beams) in the U-V plane that can be expected for the pixel located at the corner edge of the focal plane. Taking into account degradations due to using real components and with typical alignment errors, we can till expect to meet the requirements.

The design concept is illustrated in Fig.18 and the key parameters listed in Table 5. Rather than a high tower to support the focal arrangement, the plan would be to identify a suitable site in which the dish structure can be built below a cliff (or near vertical slope) of height 90 m so that the feed arrangement can be fixed on a boom near the top of the cliff.

5.2 Design for a receiver module

A high degree of stability is an essential design criterion both for telescope and receivers. Such demands are not unique since instruments used to measure the structure in the CMB have been built which meet similar stability criteria. In CMB experiments correlation receivers (or interferometers) are generally the design of choice (for example, *WMAP* and *Planck*). They can reduce the effect of gain fluctua-

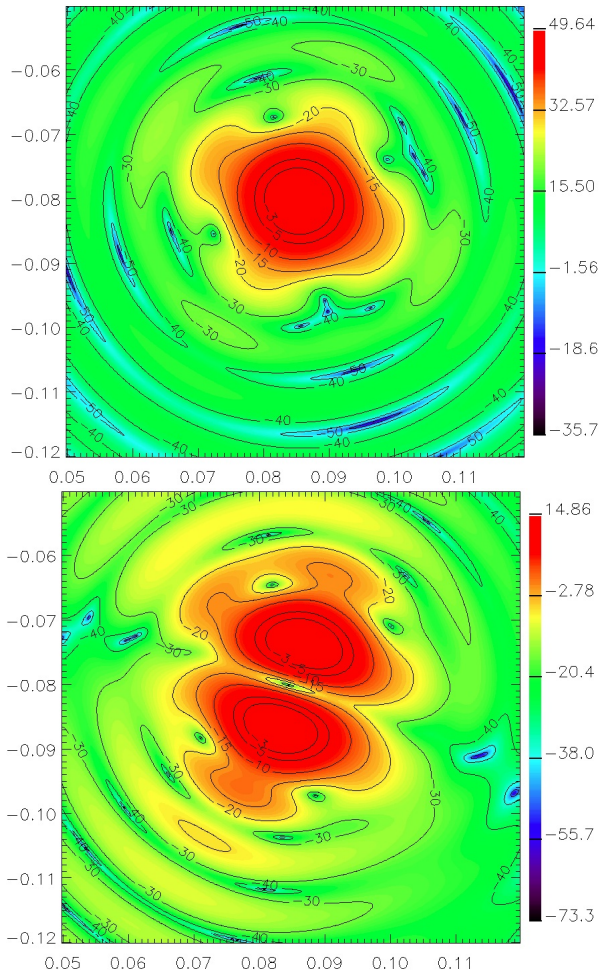


Figure 17. U-V maps of beam intensity for the most off-axis pixel corresponding to the focal plane position $x = -8\text{ m}$ and $y = -7.5\text{ m}$ (represented in red in Fig 16). Top: co-polarisation; bottom: cross-polarisation. Simulations performed using ideal telescope and horn. Colour scale: the gain in dB relative to maximum.

tions in the amplifiers ($1/f$ noise) by up to three orders of magnitude (Mennella et al. 2010).

We plan to adopt the same approach with each receiver module producing a “difference spectrum” between the desired region of sky and a reference signal. The choice of the reference is important. Ideally it should have the same spectrum as the sky and be close to the same brightness temperature. It must also be very stable. An obvious choice is another part of the sky. We propose that there should be a reference antenna for each module with a beamwidth of around 20° which would have a beam area sufficiently large to average out all but the lowest ℓ modes (see Fig. 2). It should be fixed and we suggest that it should point directly to one of the celestial poles. In this way all measurements at all times of day, and all the year round, would then be compared to the same region of sky. Since the sky emission has significant linear polarization ($\sim 10\%$ or more; Wolleben et al. (2006)), measuring with circularly polarized feeds is necessary. Similar considerations will be important for foreground emission removal. A schematic diagram for a single

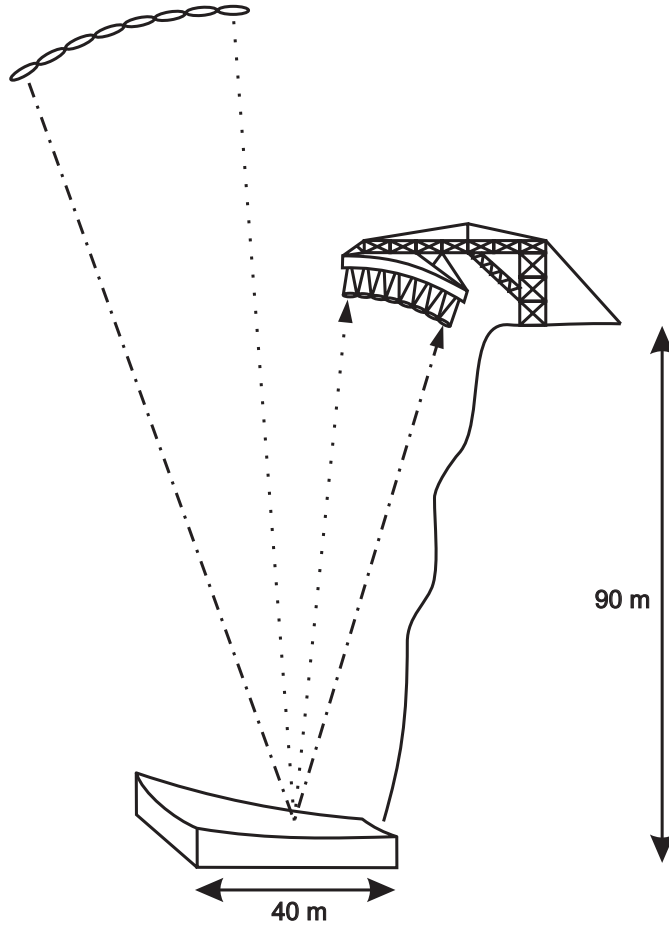


Figure 18. Schematic of the proposed design of the BINGO telescope. There will be an under-illuminated ~ 40 m static parabolic reflector at the bottom of a cliff which is around ~ 90 m high. At the top of the cliff will be placed a boom on which the receiver system of 60 feed-horns will be mounted.

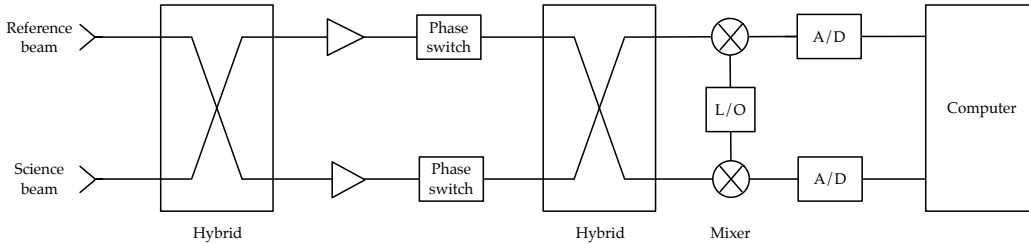


Figure 19. Block diagram of the receiver chain. The reference beam will point towards one of the Celestial Poles. The hybrids will be waveguide magic tees. After the second hybrid the signal will be down-converted using mixers with a common local oscillator. There will be further amplification before digitization.

polarization channel of the proposed receiver module design is shown in Fig. 19.

5.3 Receiver simulations

An ideal correlation receiver - one with perfectly matched system temperatures and no imbalance in the power splitting within each hybrid - can effectively remove all $1/f$ noise from its signal output. If $A = A_{\text{sys}} + \delta A$ and $B = B_{\text{sys}} + \delta B$ are the total voltages entering the receiver chain and $A_{\text{sys}} \propto$

$\sqrt{T_{\text{sys}}^A}$ and $B_{\text{sys}} \propto \sqrt{T_{\text{sys}}^B}$ are the system temperature contributions and δA and δB are the signals we want to detect, then the difference detected power at the end of the chain is proportional to the difference, $\delta A^2 - \delta B^2$, between the science (A) and reference beam (B). The spectrum of such a signal exhibits no excess power at low frequencies ($1/f$ noise) as illustrated in Fig. 20(a), and integration can continue indefinitely with the white noise falling as the square root of integration time.

However, real life receivers are imperfect. Imbalances

between system temperature and power splitting both limit the reduction of the $1/f$ noise resulting in a break in the power spectrum quantified in terms of a knee frequency (Seiffert et al. 2002) separating white noise-dominated and pink noise-dominated parts of the spectrum. Consequently there will be a limit to the viable integration time as illustrated in Fig. 20(b). It is useful to quantify by how much a correlation receiver is limited by these imperfections, and to do so we simulate their effect in a realistic receiver model. We assess the maximum permissible imperfection amplitude to ensure the knee frequency remains below $f_{\text{knee}} \sim 1$ mHz, a value corresponding ~ 20 minutes integration time - sufficient for the largest HI structures we are interested in detecting, \sim a few degrees, to drift through the telescope beam.

We include Gaussian (white) and $1/f$ noise, generating the former using a simple random number procedure and the latter with a more complex *auto-regressive* approach - essentially filtering a white noise time stream into one with correct correlation properties. The knee frequency of component amplifiers depends on both the physical choice of amplifier and the channel bandwidth. Though the actual value will need to be determined empirically, we will assume in the current simulations that the individual amplifier knee frequencies are $f_{\text{knee}}^{\text{amp}} \sim 1$ Hz for a channel bandwidth of 1 MHz.

5.3.1 Unbalanced T_{sys}

In an ideal receiver the two channels, A_{sys} and B_{sys} , should be perfectly matched. This is impossible to achieve at all times due to the angular variations in the Galactic emission and here we investigate the effect on the knee frequency due to small imbalances between the temperatures.

Modelling the entire correlation receiver and simulating noise spectra for the output difference signal in the presence of small temperature imbalances, we find that the knee frequency of the correlation receiver can be approximated by $f_{\text{knee}} = 1.2 \text{ Hz} ((A_{\text{sys}} - B_{\text{sys}})/A_{\text{sys}})^2$ and therefore to ensure BINGO's knee frequency remains continually below the desired $f_{\text{knee}} \sim 1$ mHz, our simulations show that $(A_{\text{sys}} - B_{\text{sys}})/A_{\text{sys}}$ needs to be < 0.03 . In practice the balance can be maintained electronically so this should not be an important limitation, provided the unbalance behaves predictably as a function of time. The main source of imbalance in the system temperatures will arise from the changing sky background as the telescope scans across the sky. Typical variations in those parts of the sky of interest well away from the Galactic plane will be a few Kelvin and will be repeatable from day to day. Importantly the sky emission will be spectrally smooth and virtually identical in all frequency channels. This means that once the frequency-averaged variation of sky brightness has been measured over the course of a sidereal day, a multiplicative correction, the r -factor defined by (Seiffert et al. 2002), can be applied to all channels to bring the A and B outputs into balance before differencing, thus ensuring the $(A_{\text{sys}} - B_{\text{sys}})/A_{\text{sys}} < 0.03$ is met.

5.3.2 Power Split Imbalance

We now consider the case of hybrids in which the power splitting is imperfect. To do so, we introduce the constant

coefficient ϵ , representing an imbalance between the power emerging from the two output ports of the hybrids. The signals emerging from such a hybrid are then

$$\begin{aligned} A_{\text{out}} &= \sqrt{\frac{1-\epsilon}{2}}A + \sqrt{\frac{1+\epsilon}{2}}B, \\ B_{\text{out}} &= \sqrt{\frac{1+\epsilon}{2}}A - \sqrt{\frac{1-\epsilon}{2}}B, \end{aligned} \quad (40)$$

where A, B are the two input signals.

Here we assume the power splitting imbalances in the first and second hybrids are equal, and simulate noise spectra for different values of ϵ . Fitting for the knee frequency we find $f_{\text{knee}} = 4\epsilon^2 \text{ Hz}$. Again, in order to maintain a knee frequency of 1 mHz, this relationship implies that the power splitting imbalance should satisfy $\epsilon < 0.015$. This requirement can be relaxed if a 180° phase switch is used within the hybrid loop and, since waveguide magic-tees typically have a power split imbalance of $\epsilon = 0.02$, the required performance should be achievable.

5.4 Practicalities

Our philosophy is to choose simplicity while keeping in mind good engineering practice and, wherever possible, to adopt conventional solutions to problems rather than try to invent new ones.

To reduce the impact of RFI the telescope would need to be in a remote site and therefore an important additional consideration is that everything should be easy to maintain. The design, construction and mounting of the feeds is perhaps the most challenging aspect of the overall concept. As stated above, low sidelobe levels are important in order to mitigate the effects of RFI (even in the remotest part of the World) and ease the separation of foreground emission from the desired neutral hydrogen signal. If a conventional horn design is adopted, these horns will have to be extremely large; to illuminate a 30 m dish from a focus ~ 75 m away will require an aperture diameter for each feed of 1.5 to 2 m and a length of ~ 8 m. Such feeds are practical, in the sense that they would be scaled up versions of horns built to existing feed designs, but could prove expensive to build and unwieldy. Alternatives like using small secondary mirrors for each receiver module are under consideration.

An integral part of the feed system is the extraction of polarized signals which we will do by extracting the two opposite circular polarizations. Minimizing any Ohmic loss before the first amplifiers is essential if good thermal noise performance is to be achieved. After the feed the next element is the hybrid. Due to their low loss and good power splitting properties we would use waveguide magic-tees.

We would use non-cryogenic low noise amplifiers because at this frequency the noise advantages of cooling to ~ 20 K are outweighed by the low cost, the low power consumption and the low maintenance demands of a non-cryogenic approach. It would also be desirable to integrate the amplifiers with the magic-tee to avoid the necessity to use potentially lossy cables. Some cooling, perhaps using Peltier coolers, could be used because it would provide both temperature stabilization for the amplifiers and a potential improvement in noise performance.

An important choice is when to digitize the signal. In

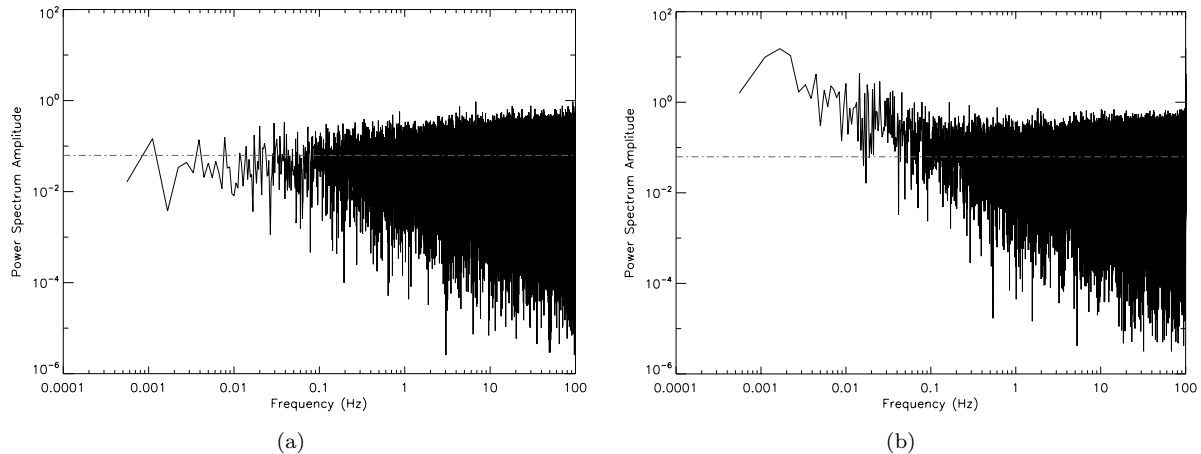


Figure 20. Simulated noise power spectra for a realistic BINGO receiver which uses amplifiers with $f_{\text{knee}} = 1$ Hz and a 30 min integration. Here (a) represents a perfectly balanced receiver; and (b) a receiver with imbalances in both system temperature, $(A_{\text{sys}} - B_{\text{sys}})/A_{\text{sys}} = 0.2$ and power splitting, $\epsilon = 0.4$. These values are significantly larger than expected in a realistic situation and have been chosen to illustrate the point. The upturn of the spectrum in (b) indicates the presence of $1/f$ noise.

conventional correlation receivers the “correlation” is performed in a second hybrid. Our preferred solution is to down-convert the radio frequency signal with a common local oscillator and then to digitize and perform the function of the second hybrid in software using FPGAs to multiply the signals and produce averaged spectra which can then be differenced. One advantage of such a system is that the levels in the two arms of the receiver can be easily adjusted so that they are the same and this then operates the receiver at its optimum for gain fluctuation reduction.

6 CONCLUSIONS

Intensity mapping is an innovative idea which has been suggested to allow large-scale structure surveys using the 21cm line of neutral hydrogen using instruments with relatively small collecting area compared to the SKA. Such concepts would naturally be much cheaper. We have presented calculations that illustrate the characteristics of the signal and it is shown that it should have an r.m.s. of $\sim 100 \mu\text{K}$ on angular scales ~ 1 deg and bandwidths of 1 – 10 MHz. At very low redshifts there will be a shot noise effect due to it being dominated by individual galaxies, at medium redshifts it is dominated by the effects of HI in galaxy clusters and at high redshifts becomes an unresolved background.

We have performed an optimisation analysis which suggests that a significant measurement of the acoustic scale can be made between $z = 0.13 - 0.48$ using a single dish telescope of diameter 40 m with a drift scan survey of a strip with width 10 deg covering a total of $\sim 2000 \text{ deg}^2$. In order to do this at higher redshift (specifically, the case of $z = 0.58 - 1.47$) would require a much larger dish, ~ 140 m, and an area of 500 deg^2 which would probably be best done using an interferometer in order to allow non-drift scan observations using such a long baseline instrument. We have presented a detailed assessment of the likely foregrounds and conclude that there will be continuum fluctuations with an r.m.s of $\sim 100 \text{ mK}$ on degree scale, but that this should not

significantly affect our ability to extract the HI signal due to the fact that its spectral profile is expected to be relatively smooth.

We have put forward a design concept, which we have named BINGO, to perform the lower of the two redshift surveys studied. This will use a large focal length telescope, $F/D \approx 2.3$, to mount an array of 60 feedhorns approximately 90 m above a static 40 m. It will use pseudo-correlation receivers to reduce $1/f$ noise due to gain fluctuations. We are currently searching for a site and the funding needed to bring this idea to fruition.

ACKNOWLEDGEMENTS

We thank Peter Dewdney for suggesting the use of a cliff to mount the BINGO feeds and Xiang-Ping Wu for suggesting using one of the Celestial Poles as a reference. We have had numerous useful discussions with Peter Wilkinson, Shude Mao and Richard Davis. CD acknowledges an STFC Advanced Fellowship and an EC IRG grant under the FP7. AP is supported by the project GLENCO, funded under the FP7, Ideas, Grant Agreement n. 259349 and also received support from the STFC(UK). We thank Bob Watson for help in creating Fig. 18.

REFERENCES

- Abbott, T. et al., 2005, [arXiv:astro-ph/0510346](#)
- Abdalla, F. B. and Rawlings, S., 2005, *MNRAS*, 360, 27
- Abdalla, F. B., Blake, C. and Rawlings, S., 2010, 401, 734
- Afshordi, N. and Loverde, M., 2008, *Phys. Rev. D* 78, 123506
- Anderson L. et al., 2012, [arXiv:1203.6594](#)
- Battye, R. A., Davies, R. D. & Weller, J., 2004, *MNRAS*, 355, 1339
- Beutler, F., Blake, C., Colless, M., et al. 2011, *MNRAS*, 416, 3017

- Blake, C. A., Davis, T., Poole, G., et al. 2011, MNRAS 415, 2892
- C. Blake and K. Glazebrook, *Astrophys. J.* **594** (2003) 665
- K. Glazebrook & C. Blake, 2005, *Astrophys. J.* **631** 1
- Bondi, M., Ciliegi, P., Zamorani, G., et al. 2003, *A&A*, 403, 857
- Bonvin, C., Durrer, R., 2011, *Phys. Rev.* **D84** 063505
- M. Bowden *et al.*, *Mon. Not. Roy. Astron. Soc.* **349** (2004) 321
- E. F. Bunn and M. J. . White, *Astrophys. J.* **480** (1997) 6
- S. M. Carroll, W. H. Press and E. L. Turner, *Ann. Rev. Astron. Astrophys.* **30** (1992) 499.
- Chang, T. -C., Pen, U. -L., Peterson, J. B. et al. 2008, *Phys. Rev. Lett.*, 100, 1303
- Challinor, A., Lewis, A., 2011, *Phys. Rev.* **D84** 043516
- Chang, T. -C., Pen, U. -L., Bandura, K. et al. 2010, *Nature*, 466, 463
- Chon, G., Challinor, A., Prunet, S., Hivon, E., & Szapudi, I. 2004, MNRAS, 350, 914
- Ciliegi, P., McMahon, R. G., Miley, G., et al. 1999, MNRAS, 302, 222
- Clifton, T., Ferreira, P. G., Padilla, C., et al. 2011, [arXiv:1106.2476](#)
- Cole, S., Percival, W. J., Peacock, J. A., et al. 2005, MNRAS, 362, 505
- Condon, J. J., Cotton, W. D., Greisen, E. W., et al. 1998, *AJ*, 115, 1693
- Copeland, E. J., Sami, M., Tsujikawa, S., 2006, *IJMPD*, 15, 1753
- Davies, R. D., Watson, R. A., & Gutierrez, C. M. 1996, MNRAS, 278, 925
- Davies, R. D., Dickinson, C., Banday, A. J., et al. 2006, MNRAS, 370, 1125
- Dickinson, C., Davies, R. D., & Davis, R. J. 2003, MNRAS, 341, 369
- Draine, B. T., & Lazarian, A. 1998, *ApJ*, 508, 157
- Duffy, A. R., Battye, R. A., Davies, R. D., et al. 2008, MNRAS, 383, 150
- Duffy, A. R., Kay, S. T., Battye, R. A., Booth, C. M., Dalla Vecchia, C., Schaye, J., 2012, 420, 2799
- D. J. Eisenstein and W. Hu, *Astrophys. J.* **496** (1998) 605
- Eisenstein, D. J., Hu, W., Tegmark, M., 1998, *ApJ*, 504, L57
- Eisenstein, D. J., Annis, J., Gunn, J. E., et al. 2001, *Astrophys. J.*, 122, 2267
- Eisenstein, D. J., 2003, in Dey, A. (Ed), *Wide-field Multi Object Spectroscopy*, ASP Conference Series
- Eisenstein, D. J., Zehavi, I., Hogg, D. W., et al. 2005, *ApJ*, 633, 2
- Feldman, H., Kaiser, N., Peacock, J., 1995 *AJ* 426, 23
- Finkbeiner, D. P., Davis, M., & Schlegel, D. J. 1999, *ApJ*, 524, 867
- Fixsen, D. J., Kogut, A., Levin, S., et al. 2011, *ApJ*, 734, 5
- Fomalont, E. B., Kellermann, K. I., Cowie, L. L., et al. 2006, *ApJS*, 167, 103
- Furlanetto, S. R., Oh, S. P., Briggs, F. H., 2006, *Phys. Rep.*, 433, 181
- Giardino, G., Banday, A. J., Górski, K. M., et al. 2002, *A&A*, 387, 82
- Grupponi, C., Ciliegi, P., Rowan-Robinson, M., et al. 1999, MNRAS, 305, 297
- Haslam, C. G. T., Salter, C. J., Stoffel, H., & Wilson, W. E. 1982, *A&ASS*, 47, 1
- Hawken, A. J., Abdalla, F. B., Hütsi, G., Lahav, O., 2011, [arXiv:1111.2544](#)
- Hopkins, A., Afonso, J., Cram, L., & Mobasher, B. 1999, *ApJL*, 519, L59
- Ibar, E., Ivison, R. J., Biggs, A. D., et al. 2009, MNRAS, 397, 281
- Jarosik, N. et al. 2011, *ApJS*, 192, 14
- Kellermann, K.I., Paulint-Toth, I.I.K., Davis. M.M., 1968, *ApL*, 2, 105
- Knox, L. 1995, *Phys. Rev. D*, 52, 4307
- Komatsu, E. et al. 2011, *ApJS*, 192, 18
- Laureijs, R. et al. 2011, [arXiv:1110.3193](#)
- Limber, D.N., 1953, *ApJ*, 117, 134
- Liu, A., & Tegmark, M. 2011, *Phys. Rev. D*, 83, 103006
- Loeb, A. & Wyithe, J.S.B., 2008, *Phys. Rev. Lett*, 100, 161301
- Martin, A.M., Giovanelli, R., Haynes, M.P., Guzzo, L., 2012, *ApJ*, 750, 38
- Mennella, A., Bersanelli, M., Butler, R. C., et al. 2010, *A&A*, 520, A5
- Meyer, M. J., Zwaan, M. A., Webster, L., et al. 2004, MNRAS, 350, 1210
- Mezger, P. G. & Henderson A. P., 1967, *ApJ*, 147, 471
- Mitchell, K. J., & Condon, J. J. 1985, *AJ*, 90, 1957
- R. P. Norris, A. M. Hopkins, J. Afonso, S. Brown, J. J. Condon, L. Dunne, I. Feain, R. Hollow, M. Jarvis, M. Johnston-Hollitt, E. Lenc, E. Middelberg, P. Padovani, and other 44 authors, 2011, *PASA*, 28, 215
- Obreschkow, D., Croton, D., Lucia, G., Khochfar, S., Rawlings, S., 2009, *ApJ*, 698, 1467
- Obreschkow, D., Klöckner, H. -R., Heywood, I., Levrier, F., Rawlings, S., 2009, *ApJ*, 703, 1890
- Overzier, R. A., Röttgering, H. J. A., Rengelink, R. B., & Wilman, R. J. 2003, *A&A*, 405, 53
- Owen, F. N., & Morrison, G. E. 2008, *AJ*, 136, 1889
- Pen, U.-L., Staveley-Smith, L., Peterson, J., Chang T.-C. 2009, MNRAS, 394, L6
- Percival, W. J., Baugh, C. M., Bland-Hawthorn, J., et al. 2001, MNRAS, 327, 1297
- Percival, W. J., et al. 2002, MNRAS, 337, 1068
- Percival, W. J., Reid, B. A., Eisenstein, D. J., et al. 2010, MNRAS, 401,2148
- Perlmutter, S., et al., 1999, *ApJ*, 517, 565
- Peterson, J.B., Bandura, K., Pen, U.-L., 2006, in *proceedings of 41st Recontres de Moriond: Contents and Structure of the Universe*
- Platania, P., Burigana, C., Maino, D., et al. 2003, *A&A*, 410, 847
- Prochaska J.X., Wolfe A.M., 2009, *ApJ* 696, 1543
- Reich, P., & Reich, W. 1988, *A&ASS*, 74, 7
- Riess, A. G., et al., 1998, *ApJ*, 116, 3
- Richards, E. A. 2000, *ApJ*, 533, 611
- Roberts, M. S., 1974, *Science*, 183, 371
- Rohlfs, K., & Wilson, T. L. 2004, *Tools of radio astronomy*, 4th rev. and enl. ed., by K. Rohlfs and T.L. Wilson. Berlin: Springer, 2004,
- Schlegel, D. et al., 2011, [arXiv:1106.1706](#)
- Scott, D., & White, M. 1999, *A&A*, 346, 1
- Seiffert, M.; Mennella, A.; Burigana, C.; Mandolesi, N.; Bersanelli, M.; Meinhold, P.; Lubin, P. 2002 *A&A*, 391, 1185

- Seiffert, M., Fixsen, D. J., Kogut, A., et al. 2011, *ApJ*, 734, 6
- Seo, H.-J., & Eisenstein, D. J. 2003, *ApJ*, 598, 720
- Seo H.-J., Dodelson, S., Marriner, J., McGinnis, D., Stebbins, A., Stoughton, C., Vallinotto, A. 2010, *ApJ*, 721, 164
- Seymour, N., Dwelly, T., Moss, D., et al. 2008, *MNRAS*, 386, 1695
- Springel, V. et al. 2005, *Nature*, 435, 629
- Szapudi, I., Prunet, S., & Colombi, S. 2001, *ApJL*, 561, L11
- Tegmark, M. 1996, *MNRAS*, 280, 299
- Vernstrom, T., Scott, D., & Wall, J. V. 2011, *MNRAS*, 415, 3641
- Weinberg D.H. et al. 2012, [arXiv:1201.2434](https://arxiv.org/abs/1201.2434)
- White, R. L., Becker, R. H., Helfand, D. J., & Gregg, M. D. 1997, *ApJ*, 475, 479
- Wilkinson, P. N., 1991, in *Proceedings of the 131st IAU Colloquium, ASP Conference Series*, 19, 428
- Wolleben, M., Landecker, T. L., Reich, W., & Wielebinski, R. 2006, *A&A*, 448, 411
- Zwaan, M. A., Meyer, M. J., Staveley-Smith, L., Webster, R. L., 2005, *MNRAS*, 359, L30